Cement and Concrete Composites 146 (2024) 105402

Contents lists available at ScienceDirect

Cement and Concrete Composites

journal homepage: www.elsevier.com/locate/cemconcomp

Effect of pore water pressure on mechanical performance of recycled aggregate concrete under triaxial compression

Yunan Li [a], Hanbing Zhao [b,**], Yong Hu [a], Fulin Qu [c], Dunming Zhu [a], Kejin Wang [d], Wengui Li [e,*]

[a] Faculty of Engineering, China University of Geosciences, Wuhan, Hubei, 430074, China
[b] School of Civil and Environmental Engineering, University of Technology Sydney, NSW, 2007, Australia
[c] Department of Civil and Environmental Engineering, The Hong Kong Polytechnic University, Hong Kong, China
[d] Department of Civil, Construction and Environmental Engineering, Iowa State University, IA, 50011, USA
[e] Centre for Infrastructure Engineering and Safety, School of Civil and Environmental Engineering, The University of New South Wales, Sydney, NSW, 2052, Australia

ARTICLE INFO

Keywords:
Recycled aggregate concrete (RAC)
Interfacial transition zone (ITZ)
Triaxial compression
Pore water pressure
Failure criterion
Stress-strain model

ABSTRACT

The pore water pressure in concrete can significantly increase due to volume compression. Recycled aggregate concrete (RAC) possesses a more complex microstructure compared to natural aggregate concrete (NAC). Understanding the porosity and micromechanical properties of RAC is crucial for analysing its failure mechanism under the influence of coupled confining pressure and pore water pressure. This study compares the constituent proportions and micromechanical properties of interfacial transition zones (ITZs) and the adjacent paste matrix in NAC and RAC. Compressive stress-strain curves were obtained for concrete under coupled confining pressure and pore water pressure. The results indicate that the newly formed ITZ, which bonds to old mortar, outperformed the one bonded to natural aggregate when considering the same water-cement ratio. Compressive strength, ductility, and maximum volumetric strain gradually increased with increasing confining pressure. However, when pore water pressure was removed, compressive strength decreased while elastic modulus improved. Due to the inferior microstructures of RAC compared to NAC, the supportive effect of pore water becomes more pronounced. This is evident in the gradual increase in peak strain with increased pore water pressure for the stress-strain curves of RAC (100 % replacement ratio). Finally, a failure criterion and stress-strain theoretical model considering pore water pressure are proposed, and satisfactory fitting results are obtained.

1. Introduction

The density of natural sand/gravel in normal strength concrete (NSC) is much higher than that of cement paste matrix. Due to the 'wall effect', the constituent proportion of the cement paste within 15–50 μm from the aggregate surface is obviously different from the paste matrix far from the aggregate surface [1]. This cement paste region adjacent to the aggregate surface is called the interfacial transition zone (ITZ). Experimental results show that the compactness and micromechanical properties of ITZ are generally lower than paste matrix in NSC, which means ITZ is the key to analysing the mechanism of concrete failure under external load and resistance to water permeability [2–4].

Benefit from advances in material micro/nano-level observation technology, such as Backscattered electron-Image analysis (BSE-Image analysis) technique and nanoindentation/nanoscratch, researchers can more accurately identify the width of ITZ and study the microscopic performance within ITZs [5]. Lyu et al. [6] successfully captured pores in the BSE images of cement paste according to the grey threshold value and then converted the BSE images into binary images. The difference in pore size and pore volume fraction between ITZ and paste matrix were compared in their research [6]. Nuruzzaman et al. [7] and Hosan et al. [8] determined that the width of ITZ was about 40 μm based on the contour map of the elastic modulus in the cement paste obtained from nanoindentation. Bosque et al. [9] compared the measurement results from electron microscopy and nanoindentation, and found that the ITZ width determined by the former was higher than that by the latter. Wei et al. [10] obtained continuous test data by nanoscratch, and estimated the proportion of C-S-H, CH and clinker through fracture toughness.

* Corresponding author: Centre for Infrastructure Engineering and Safety, School of Civil and Environmental Engineering, The University of New South Wales, Sydney, NSW, 2052, Australia.
** Corresponding author.
E-mail addresses: hanbing.zhao@student.uts.edu.au (H. Zhao), wengui.li@unsw.edu.au (W. Li).

https://doi.org/10.1016/j.cemconcomp.2023.105402
Received 8 August 2023; Received in revised form 24 October 2023; Accepted 4 December 2023
Available online 7 December 2023

Moreover, through the fracture mechanics theory, Wei et al. [10] combined the concept of the friction coefficient method to propose a new quantification method for ITZs.

The basic mechanical properties and durability of recycled aggregate concrete (RAC) have been comprehensively investigated. For example, Thomas et al. [11] concluded that the 28-day compressive strength reduced by 11–19 % when 100 % of natural coarse aggregate (NCA) was replaced by recycled coarse aggregate (RCA). Pedro et al. [12] indicated that the water absorption by immersion of concrete has a linear increasing relationship with RCA replacement ratio. They believe that the weak bonding performance of ITZs in RAC is responsible for the poor mechanical properties and durability of RAC [11,12].

RAC has more complicated ITZs, mainly because of the presence of old mortar on the surface of the aggregate [11,13,14]. The ITZs in RAC deserve special attention including the old ITZ between natural aggregate and old mortar and the new ITZ between old mortar and new mortar [15]. Wu et al. [16] obtained the micromechanical properties of old and new ITZs in RAC by nanoindentation. The width of the new ITZ was slightly larger than the old ITZ, while the elastic modulus of the new ITZ was 16.4 GPa lower than the old ITZ of 24.5 GPa [16]. Xiao and Li et al. [17,18] conducted a large number of tests and concluded that the micromechanical properties of old and new ITZs in RAC were closely related to the mixture proportion, mixing method and curing age of the corresponding mortar matrix.

There have been many studies on the basic mechanical properties of RAC under compression, tension, shear and impact loads [19–22]. However, concrete is generally under a multiaxial loading state, such as a triaxial compression state rather than being subjected to a simple unidirectional load during its service period [23–25]. Existing research results show that when RAC is subjected to a high lateral confinement, its compressive strength, ductility and toughness all increase significantly, and the mechanical properties difference between natural aggregate concrete (NAC) and RAC with the same water-cement ratio alleviate [26–28]. This is because lateral pressure relieves the adverse effect of the multi-ITZs on the compressive strength of RAC [27]. In addition, the cracks cannot propagate freely under the action of lateral confinement. The evidence is that the failure mode converted from vertical splitting failure under uniaxial compression to slip-shear failure mode [27,29]. The triaxial compressive strength depends more on the mechanical properties of the aggregate and mortar matrix [30]. However, some researchers pointed out that excessive confining pressure would lead to new cracks in concrete, resulting in a decrease in elastic modulus [31].

Another point worth noting is that pore water in the concrete is difficult to completely dissipate, especially for underground structures including bridge piers, dams and pile foundations [32]. The pore water pressure would emerge and increase rapidly under obvious compression deformation. The effect of pore water pressure on crack expansion and compression deformation of concrete cannot be ignored [33,34]. Researchers have realised the significance of porosity and pore pressure to study the triaxial compression properties of concrete [33,34]. He et al. [35] established a pore-cement paste finite element model through ANSYS. Experimental and numerical simulation results show that pores increased the deformation properties of concrete, and when the pore pressure was higher than 17 MPa, dense damage occurred around the pores [35]. Vu and Malecot et al. [33,34] investigated the mechanical properties of dry, semi-saturated and fully saturated concrete at confining pressure of up to 600 MPa. Pore water pressure played a major role in the triaxial compressive strength and bulk stiffness of concrete [33,34]. When the pore pressure existed, the efficiency of confining pressure to improve the compressive strength of the concrete decreased, and the deformation capacity before failure was weakened [33,34].

Up to now, no one has experimentally revealed the triaxial compressive properties of RAC in the presence of a constant pore water pressure. Wu et al. [16] pointed out that there is a superior linear relationship between the compressive strength of RAC and the micromechanical properties of the old ITZ. Xiao et al. [36] reported that the compressive strength of RAC improved with the increase of the elastic modulus of new mortar matrix by finite element simulation. However, there is still a lack of experimental data linking the microstructure, micromechanical properties and macromechanical properties of RAC under the coupling of multilevel loads [37]. Therefore, this study statistically analysed the porosity in the old and new ITZs and adjacent paste matrix of RAC through the BSE-Image analysis technique [38–40]. Nanoindentation was used to obtain the elastic modulus and hardness in the region corresponding to the BSE-Image analysis. Then, different levels of confining pressure and pore water pressure were applied to the cylindrical concrete specimens with 0 %, 50 % and 100 % RCA replacement ratios, and the stress-strain curves were obtained. Based on the existing theoretical model, the relationship between the porosity, micromechanical properties of weak regions in RAC and macromechanical properties under multi-field coupling stress state was established. The experimental data and theoretical analysis in this study in contributed to extend the application of RAC in complicated stress conditions.

2. Experimental programme

2.1. Materials and specimen preparation

The concrete specimens used for triaxial compression tests were Φ50 × 100 mm cylinders. According to the ratio requirement of concrete specimen diameter to coarse aggregate particle size in ASTM C192 (Standard practice for making and curing concrete test specimens in the laboratory), the particle size of NCA and RCA was determined to be 5–16 mm. The main physical properties of NCA and RCA are summarized in Table 1. It can be seen that the density of RCA was lower, whereas water absorption and crush index were higher due to porous old mortar attached to the surface of RCA. Natural river sand with a fineness modulus of 2.80, an apparent density of 2615 kg/m^3 and water absorption of 1.44 % was adopted as natural fine aggregate (NFA). The particle size distribution of NFA is shown in Fig. 1, which satisfies the requirements in ASTM C33. PO 42.5 ordinary Portland cement with fineness lower than 10.0 according to GB 175–2007 was mixed with water, coarse aggregate and fine aggregate for concrete specimens. Naphthalene-based superplasticizer (SP), which can improve the slump of concrete over 10 cm was used to modify the rheological behaviour of fresh concrete mixture.

RCA replacement ratio was 0 %, 50 % and 100 %. Considering that the density difference between NCA and RCA is within the acceptable range, the percentage here is the mass-based replacement ratio. The detailed mixture proportion of NAC and RAC are shown in Table 2. The weighted NCA and RCA according to Table 2 were soaked in water for 24 h and kept in a saturated surface dry (SSD) state before the formal mixing to compensate the high-water absorption of RCA. After all the raw materials were ready, coarse and fine aggregate was poured into a drum mixer and dry-mixed for 1 min. Then, cement was poured into the drum mixer and dry-mixed with aggregate for another 1 min. Finally, the water mixed with SP was poured into the mixer slowly and evenly. The mixer continued to work for 2–3 min until all constituents were mixed uniformly. When the mixing was done, slump tests were conducted immediately. The slump of RAC was slightly higher than that of NAC, because the RCA contained more absorbed water in the SSD state,

Table 1
Physical properties of coarse aggregate.

	NCA	RCA
Size (mm)	5–16	5–16
Apparent density (kg/m^3)	2791.5	2736.5
Water absorption (wt. %)	1.375	5.910
Crush index (wt. %)	17	22

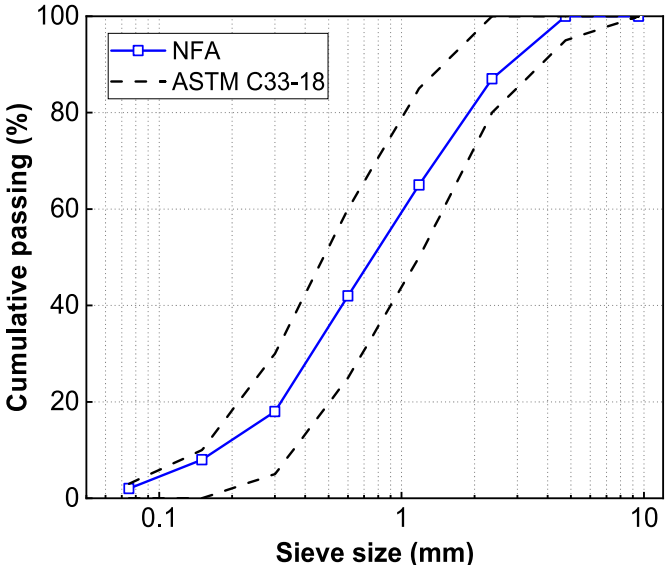

Fig. 1. Particle size distribution of fine aggregate.

Table 2
Concrete specimen mix proportions.

Mix	Raw materials (kg/m^3)					
	NCA	RCA	NFA	Cement	Water	SP
NAC	1055	0	675	498	174	4.23
RAC50	527.5	527.5	675	498	174	4.23
RAC100	0	1055	675	498	174	4.23

Note: Aggregate and cement are both in a dry state.

but the slump was at 120–140 mm.

The fully mixed fresh concrete mixtures were cast in Φ50 mm × 100 mm cylinder moulds and consolidated by a vibration table for about 30s until no large bubbles emerged. The top surfaces of the concrete samples were covered with a plastic film to prevent water evaporation. After curing in the moulds for one day, the solidified concrete specimens were transferred to a standard curing room (25 ± 5 °C, 95 % RH) for one year.

2.2. Sample preparation for microstructure and nanoindentation tests

A cylindrical concrete specimen was randomly selected and cut into small slices from the middle. Then, the concrete slice containing RCA and new mortar was placed into a Φ35 mm cylindrical mould, followed by pouring epoxy resin. After the epoxy resin was solidified, the surface of sample was ground by 120, 240, 600 and 1200 grit abrasive paper for 10 min each [41,42]. The sample surface was then polished by 0.3 μm and 0.05 μm alumina suspensions for 30 min each [41,42]. After each polishing, the sample was put into an ultrasonic bath for 2 min cleaning to remove the alumina particles attached to the surface. Finally, the processed sample was dried in a vacuum oven at 60 °C for 48 h.

2.3. BSE-based image analysis

NAC and RAC slice samples coated with epoxy resin were used to observe the pore structure of ITZs by a scanning electron microscope (SEM, Zeiss EVO LS15). The accelerating voltage was set as 15 kV. To enhance the conductivity of the sample, the sample was sputter-coated with a layer of 5 nm platinum. At least 30 BSE images at a magnification of 500× were obtained at constant contrast and brightness for each ITZ.

The volume fraction of constituents in ITZs and the adjacent paste matrix can be obtained by grey level analysis by Image Pro [43,44]. The interface between aggregate and cement paste was captured and 17 strips with 5 μm in width were taken from aggregate to paste matrix. The width of ITZ was determined by the distribution of unreacted products [41]. As a result, the porosity of ITZ and adjacent paste matrix in each BSE image can be obtained.

2.4. Nanoindentation tests

A Nano Indenter G200 equipped Berkovich tip was used for grid nanoindentation tests. Berkovich tip is a triangular pyramid with the same aspect ratio. Based on the geometric shape of the tip, requirements in standards (ASTM E384-17) and previous research, the indentation depth was designed to be 400 nm to satisfy results accuracy and sufficient measuring points conducted within ITZs [45,46]. Fig. 2 (a) to (c) show the indentation regions of ITZ in NAC (ITZ-NAC), Old ITZ and New ITZ in RAC (old ITZ-RAC and new ITZ-RAC). Fig. 2 (d) illustrates test points distribution in each region. The vertical and lateral space between measuring points were 10 μm and 5 μm respectively. A total of 10 groups of 5 × 20 grid nanoindentation test areas were taken randomly along each ITZ. The test area artificially avoided areas near fine aggregate and cracks. When the indentation depth reached 400 nm, the tip was maintained at the maximum load for 10 s and then unloaded to 10 % of the peak load. The elastic modulus and hardness of ITZs can be obtained by the following equations:

$$H = \frac{P_{max}}{A} \tag{1}$$

$$S = \frac{dP}{dh}\bigg|h = h_{max} = \frac{2}{\sqrt{\pi}} E_r \sqrt{A} \tag{2}$$

$$\frac{1}{E_r} = \frac{1-\nu^2}{E} + \frac{1-\nu_i^2}{E_i} \tag{3}$$

where, E and H are elastic modulus and hardness respectively. P is the indentation load. A represents project area. h is the indentation depth. E_r and E_i is the reduced elastic modulus and indenter tip elastic modulus respectively. ν and ν_i is the Poisson's ratio of cement paste and indenter tip respectively. The characteristics (E_i and ν_i) of the diamond indenter tip have been input in the system. Parameters P, A, h and E_r can be obtained directly from testing results. ν was set as 0.2 in this research.

2.5. Triaxial and pore pressure test

A triaxial multi-field coupled testing system (RTX-1000) was used to test the compression performance of concrete under different confining pressure and pore water pressure. The system has two Linear Variable Differential Transformers (LVDTs) and one circumferential LVDT (all with ±2.5 mm range), for measuring axial and radial strains respectively. The system has an independent servo-controlled axial pressure actuator, confining pressure actuator and pore pressure actuator, which can apply 1000 kN of axial load and 70 MPa of confining and pore pressure respectively.

Four different levels of confining pressure ($\sigma_c = \sigma_1 = \sigma_2 = 0$, 3, 7, 14 MPa) and four different level of pore pressure (σ_p = 0, 5, 9, 13 MPa) were designed in this experiment. The specific pressure parameters are shown in Table 3. Each group of tests was repeated once. Both ends of concrete specimens were ground flat with the error less than 0.1 mm by a grinder. To prevent the oil from being pressed into the concrete specimen, a heat shrink tube was wrapped and tightly attached to the surface of the specimen. The holes on the surface of the concrete specimen were sealed with the same water-cement ratio mortar. The triaxial compression apparatus and a sample covered with a heat shrink tube and installed LVDTs is shown in Fig. 3.

Stress states of concrete specimens and the loading procedure in the experiment are shown in Figs. 4 and 5 respectively. The uniaxial compression test ($\sigma_c = \sigma_p = 0$) was carried out at first. To ensure full

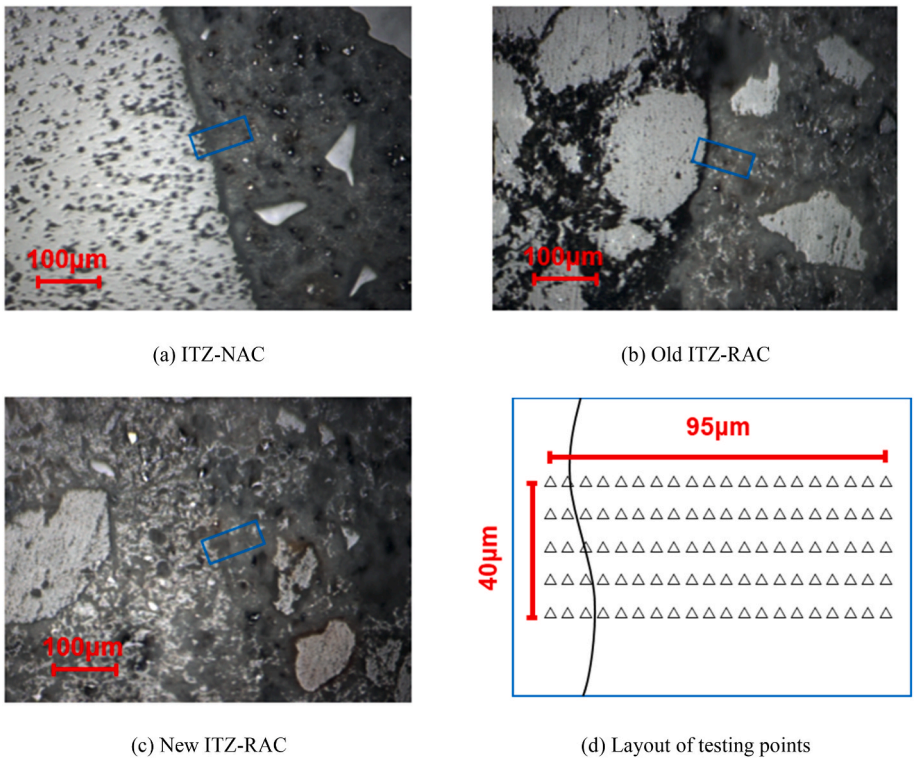

(a) ITZ-NAC (b) Old ITZ-RAC

(c) New ITZ-RAC (d) Layout of testing points

Fig. 2. Schematic of grid nanoindentation tests on ITZs.

Table 3
Testing parameters for compression.

Mix	σ_c (MPa)	σ_p (MPa)	Specimen	σ_c (MPa)	σ_p (MPa)
NAC-0	0	0	RAC50-14-5	14	5
NAC-3	3	0	RAC50-14-13	14	13
NAC-7	7	0	RAC100-0	0	0
NAC-14	14	0	RAC100-3	3	0
NAC-14-5	14	5	RAC100-7	7	0
NAC-14-9	14	9	RAC100-14	14	0
NAC-14-13	14	13	RAC100-14-5	14	5
RAC50-0	0	0	RAC100-14-9	14	9
RAC50-7	7	0	RAC100-14-13	14	13
RAC50-14	14	0			

contact between the loading panel and the top surface of specimen at the initial stage of the stress-strain curve, the specimen was loaded to 4 kN (approximately 10 % of the peak load) and maintained for 20 s. The strain control method was adopted at the rate of 0.02 %/min until radial strain reached 2 % in the subsequent compression process. For triaxial compression tests ($\sigma_c \neq 0$; $\sigma_p = 0$), concrete specimens were fixed by a 4 kN axial load. Subsequently, silicone oil was injected into the triaxial pressure cell. The axial pressure and confining pressure were simultaneously raised to the target value at 0.2 MPa/s and maintained the concrete specimen under a hydrostatic pressure condition for 20 s. Finally, the axial load was applied at 0.02 %/min until the radial strain reaching 2 %. Regarding coupled test of confining pressure and pore water pressure ($\sigma_c \neq 0$; $\sigma_p \neq 0$), to make the internal pore pressure uniform, concrete specimens were vacuum-saturated for 24 h before the formal test. Preloading and hydrostatic pressure condition steps were same with triaxial compression tests. Pure water was injected from the top of the concrete specimen to the bottom at designed pore water pressure as shown in Fig. 6. After loading the pore water pressure, the water outlet was closed and maintained for 4 h to ensure a stable pore water pressure. Finally, the axial load continued rising at a rate of 0.02 %/min until the radial strain reaching 2 % and the stress-strain curves were obtained. It should be noted that confining pressure and pore water

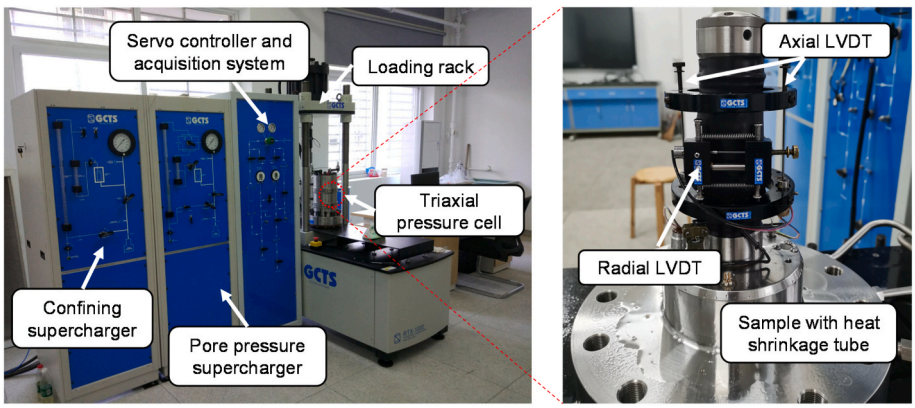

Fig. 3. Triaxial testing apparatus for concrete specimens.

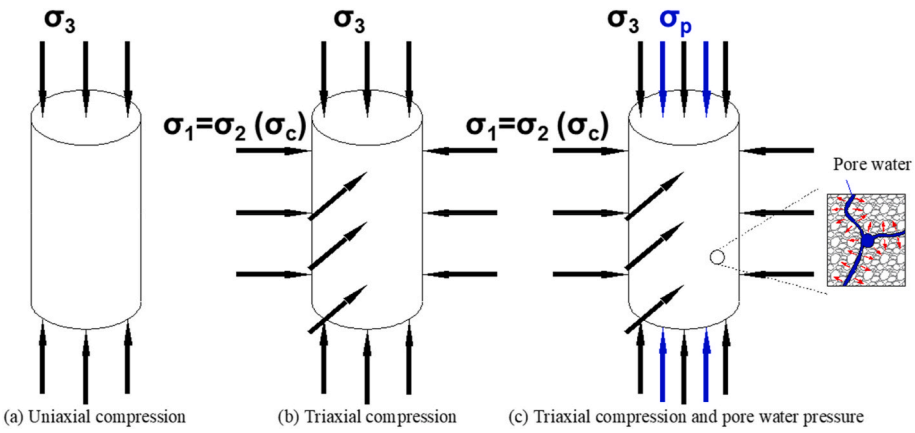

Fig. 4. Stress states of concrete specimens.

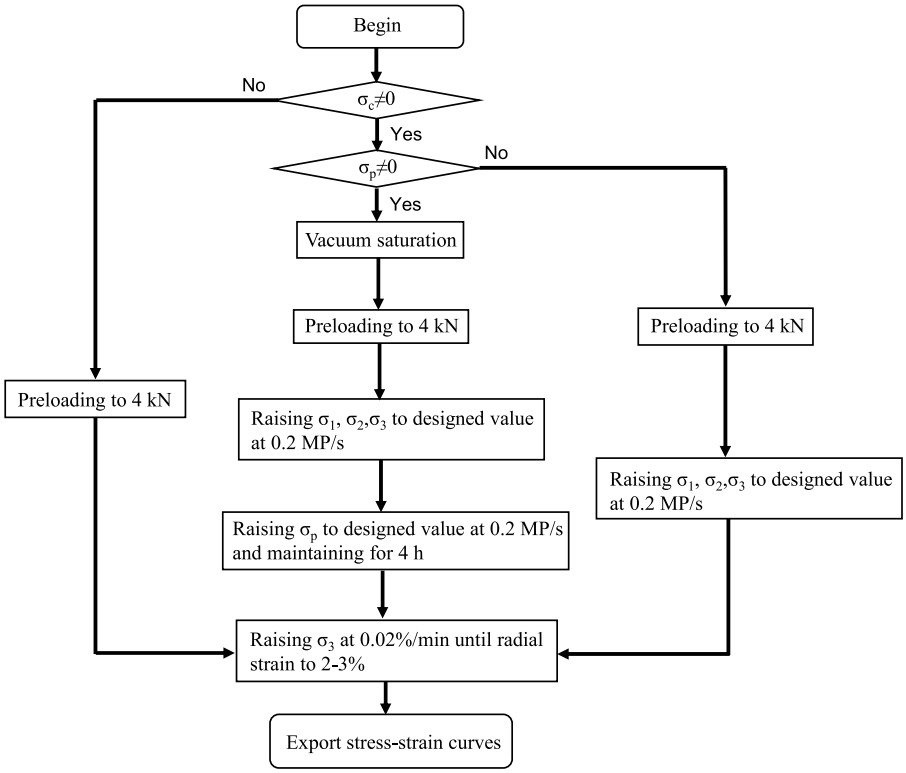

Fig. 5. Flow chart of loading scheme.

pressure were monitored in real time to ensure they are maintained at designed value during compression.

3. Results and discussions

3.1. ITZs identification

The ITZ width of concrete can be identified from the area in the BSE images where the content of unreacted products or reaction products changes significantly. Fig. 7 (a) to (c) are the BSE images of three ITZs in this study. According to the grey threshold theory proposed by Wong et al. [43,44,47], the unreacted product with the highest grey value was captured and replaced by white areas. The cement paste was divided into 17 consecutive 5 μm-width bands starting from the interface. According to previous identification results, the ITZ width of concrete was between 15 and 50 μm [3,48,49]. Therefore, it can be speculated that the segmented region contains the entire ITZ and part of paste matrix. For each type of ITZ, at least 30 different BSE images were used to statistical analyse the variation of unreacted product content at different distances from the aggregate boundary. The statistical results are shown in Fig. 8.

The trend of unreacted product content in Cement paste-NAC and Old cement paste-RAC with the distance from the aggregate boundary was similar. The volume fraction improved rapidly and then maintained at a stable value. As a result, it can be deduced that the width of the ITZ-NAC and Old ITZ-RAC was 17.5 μm. Due to the uneven and porous structure of the old mortar on the surface of RCA, the 'wall effect' in the new ITZ was not obvious. The content of unreacted products increased rapidly within 2.5–7.5 μm from the old mortar boundary, and then entered a slow rising stage with the increase of the distance. According to the volume fraction of unreacted products, the width of the New ITZ-RAC was about 27.5 μm. Furthermore, it is evident that the unreacted

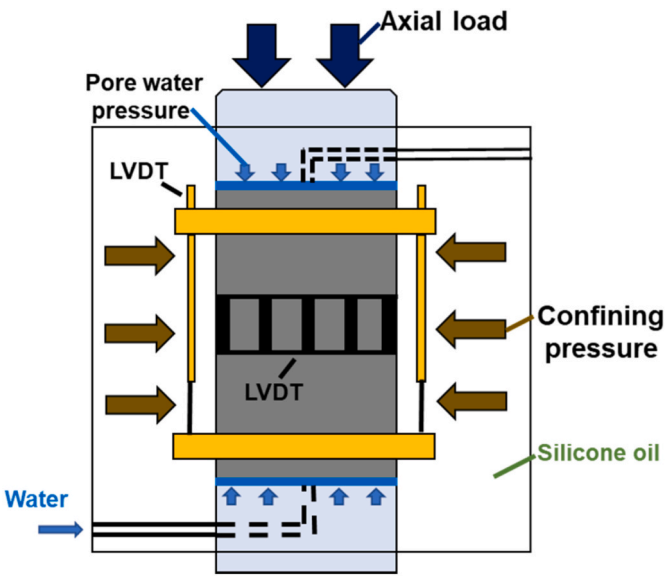

Fig. 6. Schematic diagram of loading methods.

product content in the Cement paste-NAC was higher compared to that of the New cement paste-RAC, despite the fact that the mixture design of the two pastes was the same in Table 2. The reason is probably that when the RAC was at SSD condition, the absorbed water in the RCA promoted the hydration of the unhydrated cement clinkers in the old mortar during long-term curing, and at the same time, function like an internal curing agent, the desorbed water from the RCA promoted the hydration reaction in the adjacent new cement paste. Due to the longest curing age, the content of unreacted products in the Old cement paste-RAC was the lowest.

In addition to the volume fraction of unreacted products, the width of ITZs can also be identified according to the micromechanical properties. In general, the elastic modulus of ITZ is lower than that of paste matrix. Fig. 9 shows the elastic modulus distribution of three cement paste adjacent to aggregate in this research. Similar to the distribution of unreacted products, the 'wall effect' was obvious in Cement paste-NAC and Old cement paste-RAC. The width of the ITZ-NAC and Old ITZ-RAC can be roughly identified as 12.5 μm and 22.5 μm, respectively. The elastic modulus of the new ITZ, which the width was about 32.5 μm in RAC, higher than that of the ITZ-NAC and the Old ITZ-RAC. Based on the results of image analysis and nanoindentation, the width of the ITZ-NAC, the Old ITZ-RAC and the New ITZ-RAC are finally determined as 15 μm, 20 μm and 30 μm, respectively.

3.2. Nano/micromechanical properties of ITZs

Fig. 10 shows the nanoindentation test results of NAC and RAC. Average values and standard deviations of ITZs and adjacent paste matrix are listed in Table 4. The elastic modulus of the new ITZ and paste matrix were found to be higher than those of the corresponding regions in the NAC, despite having the same water-cement ratio design value. The similar difference was also observed in the unreacted products (see Fig. 8). The elastic modulus of the new ITZ and the new paste matrix in RAC were 23.97 GPa and 24.54 GPa, which were 65.8 % and 46.6 % higher, respectively, than those in the corresponding regions in NAC. This probably because both the NCA and RCA were in an SSD state before the formal preparation of concrete. Due to the porous and cracked structure of old mortar, water retention capacity was better than NCA. During the curing process, the free water on the surface of NCA could cause an increase in the water-cement ratio of the ITZ, leading to a reduction in the elastic modulus. The absorbed water in RCA may function as an internal curing agent and old mortar in RAC continued to hydrate during the long-term curing process, which enhanced the bonding performance with the new paste. Bosque et al. [9] also pointed

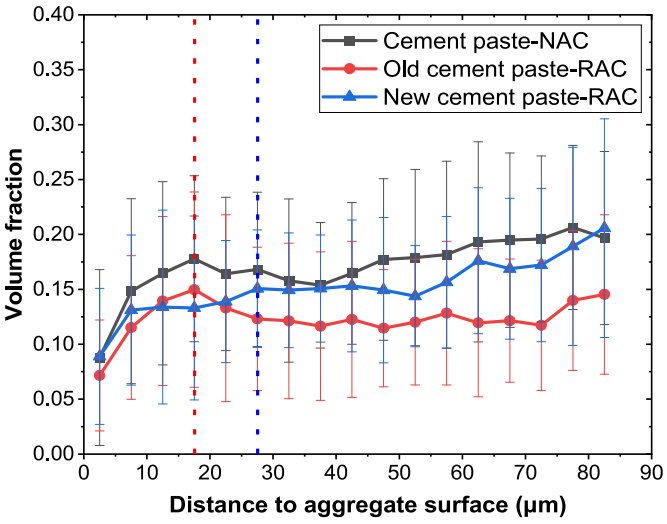

Fig. 8. Statistical results of unreacted products distribution in different ITZs.

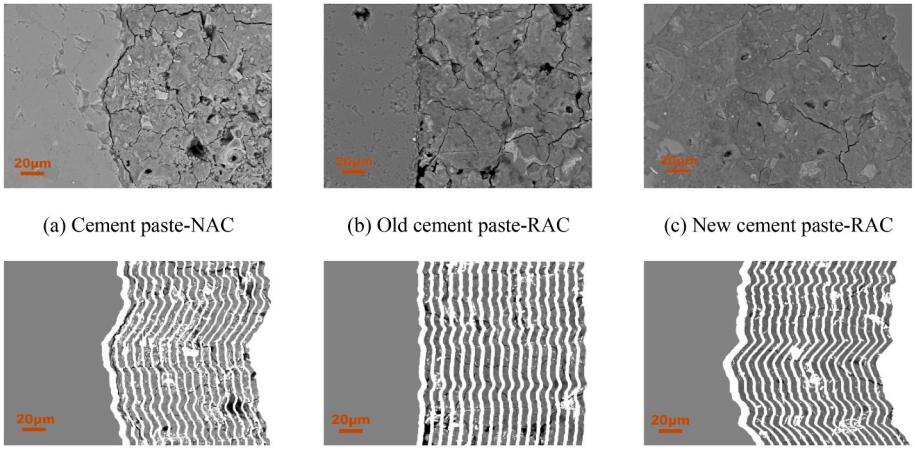

(a) Cement paste-NAC (b) Old cement paste-RAC (c) New cement paste-RAC

(d) Processed ITZ-NAC (e) Processed Old ITZ-RAC (f) Processed New ITZ-RAC

Fig. 7. Segmentation of unreacted products in ITZs and adjacent matrix.

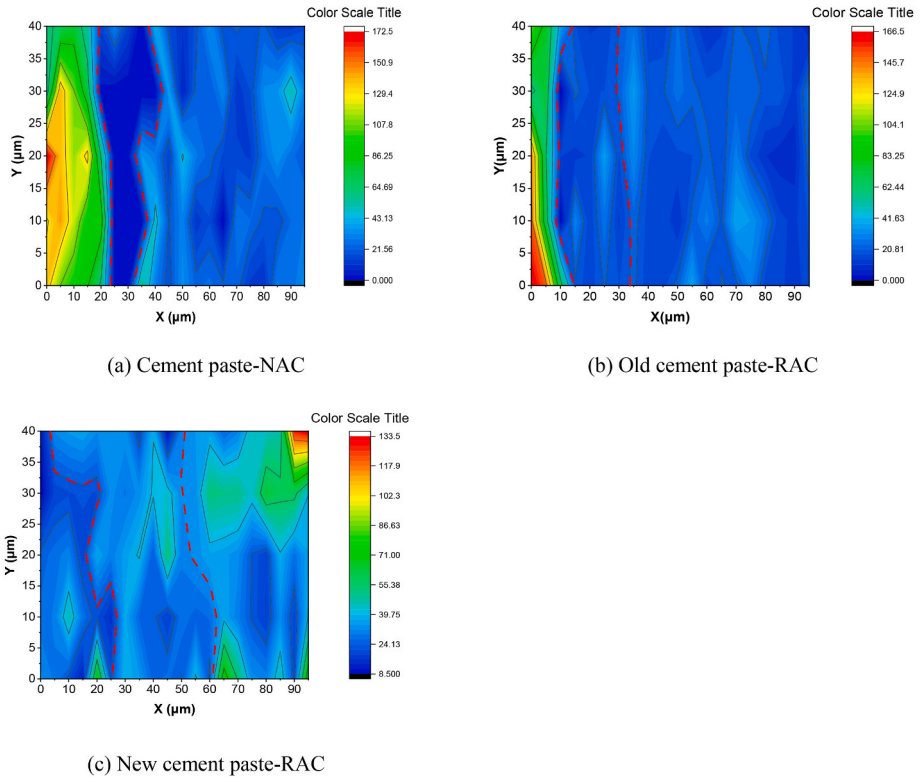

(a) Cement paste-NAC (b) Old cement paste-RAC

(c) New cement paste-RAC

Fig. 9. Elastic modulus contour map of different cement pastes adjacent to aggregate.

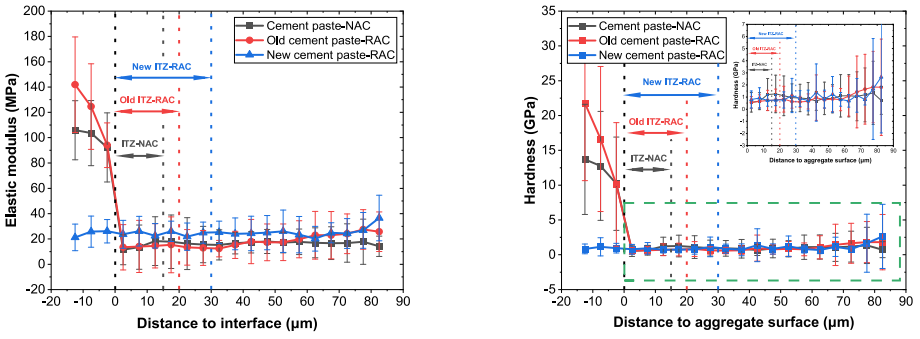

(a) Elastic modulus (b) Hardness

Fig. 10. Nanoindentation test results of different ITZs and corresponding adjacent matrix.

Table 4
Micromechanical properties of ITZs and adjacent paste matrix.

Indent regions	Micromechanical properties	
	Elastic modulus (GPa)	Hardness (GPa)
ITZ-NAC	14.46 ± 2.85	0.81 ± 0.28
Paste matrix-NAC	16.74 ± 1.06	1.01 ± 0.19
Old ITZ-RAC	14.44 ± 0.46	0.67 ± 0.07
Old paste matrix-RAC	18.52 ± 4.44	1.07 ± 0.44
New ITZ-RAC	23.97 ± 1.84	0.85 ± 0.14
New paste matrix-RAC	24.54 ± 3.25	1.16 ± 0.55

out that the micromechanical properties of ITZ were closely related to the type of interface. The elastic modulus of ITZ bonded to rough-surfaced aggregate such as asphalt, clay or recycled aggregate was higher than that of ITZ bonded to smooth-surface aggregate including glass and plastic. The elastic modulus of Old ITZ-RAC was similar to that of ITZ-NAC, both about 14.45 GPa. However, the elastic modulus of Old paste matrix-RAC was 18.52 GPa, which was 10.6 % higher than that of the Paste matrix-NAC. In comparison, the hardness of each region was similar, but the numerical difference was consistent with the elastic modulus.

3.3. Porosity and pore diameter distribution within ITZs

Fig. 11 shows the variation of pores and cracks volume fraction from ITZ to paste matrix in NAC and RAC. It is evident that the "wall effect" of the ITZ-NAC and Old ITZ-RAC in contact with NCA was the most prominent. The volume fraction of pores and cracks reached 18.7 % at a distance of 2.5 μm from the aggregate boundary, followed by rapidly dropping to a stable value. The porosity of the old ITZ and old paste matrix in RAC was higher than that of the corresponding regions in NAC. In comparison, the volume fraction of pores and cracks in the New cement paste-RAC constantly showed a stable and slightly decreasing trend with the distance from the aggregate boundary.

The pores and cracks of the ITZ and the paste matrix within 50 μm

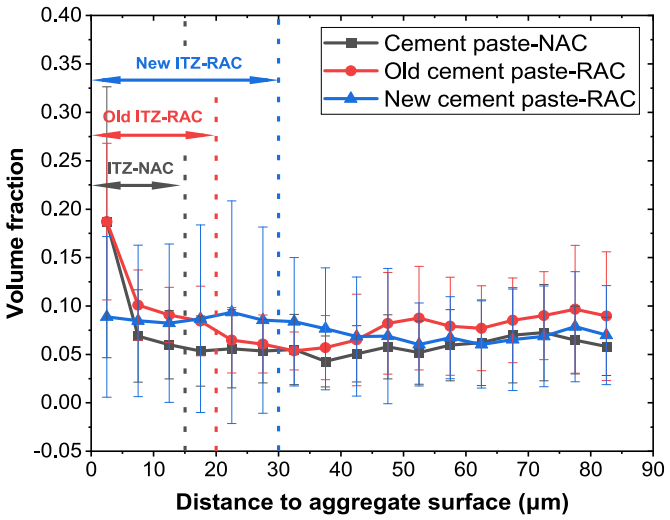

Fig. 11. Proportion statistical results of pores and cracks distribution in ITZs and adjacent matrix.

from the outside of the ITZ were captured according to the grey threshold. The equivalent circle diameter was calculated based on the area of pores and cracks. The cumulative porosity of ITZ and adjacent paste matrix in NAC and RAC was shown in Fig. 12. As seen in Fig. 12 (a), most of pores in ITZ-NAC were larger than those in Paste matrix-NAC. In contrast, there was no significant difference in old cement paste-RAC and New cement paste-RAC in each equivalent diameter range in Fig. 12 (b) and (c).

For a more detailed comparison of the pore size distribution in the ITZ and paste matrix, the proportion of pores and cracks with an equivalent diameter of 0.1–10 μm was shown in Fig. 13. No matter ITZ or paste matrix, there were three obvious peaks at 0.25 μm, 0.65 μm and 1.5 μm. Pores and cracks with equivalent diameter of approximately 0.25 μm, 0.65 μm and 1.5 μm are considered in this study as slight defects, moderate defects and severe defects, which are segmented by green, light blue and orange in Fig. 13. It can be seen that ITZ-NAC and Paste matrix-NAC possessed the lowest proportion of slight defects, which were 38.5 % and 41.1 %, respectively. However, the proportions of moderate defects (7.9 % for ITZ-NAC and 7.1 % for Paste matrix-NAC) and severe defects (10.3 % for ITZ-NAC and 9.6 % for Paste matrix-NAC) were the highest. Despite the same water-cement ratio, the proportion of slight defects in New cement paste-RAC was higher than that of Cement paste-NAC, and the proportion of moderate and severe defects was lower than that of Cement paste-NAC. The percentages of three types of defects were 44.9 %, 5.6 % and 8.0 % respectively for New ITZ-RAC and 45.0 %, 5.6 % and 7.7 % respectively for New paste matrix-RAC. As explained earlier, the bleeding phenomenon of NCA resulted in a higher proportion of large size pores and cracks in the ITZ and adjacent paste matrix. It was also pointed out in the Pope et al.'s research [50] that the porosity in the concrete ITZ depended on the relative humidity in the aggregate surface. Furthermore, it is important to note that natural aggregate lacks the secondary hydration function found in old mortar. The continuous, long-term hydration of old mortar actually enhanced the bond with new mortar. Due to longer curing age, Old ITZ-RAC had the highest percentage of slight defects, while the lowest percentages of moderate and severe defects, which were 46.4 %, 5.2 % and 7.0 %, respectively. Similarly, the proportions of the three kinds of defects in Old paste matrix-RAC were 46.6 %, 5.3 % and 7.8 %, respectively.

The average percentages of pores and cracks, unreacted products, and reacted products in the ITZ and corresponding paste matrix obtained through image analysis are listed in Table 5. For pores and cracks in ITZ and paste matrix, consistent with the above results, the average volume fraction of ITZ-NAC was 1.83 % higher than New ITZ-RAC. However, as the distance from the aggregate boundary increases, the influence of free water attached to the aggregate surface weakened, and

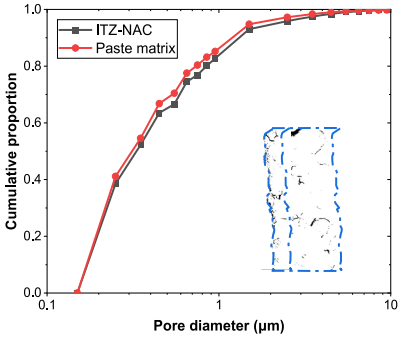

(a) Cement paste-NAC

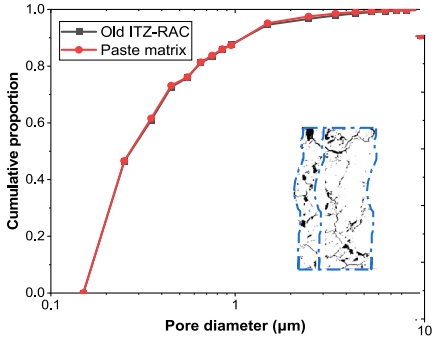

(b) Old cement paste-RAC

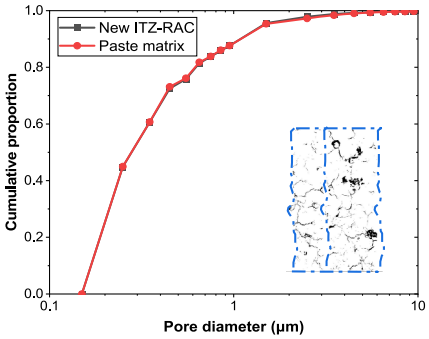

(c) New cement paste-RAC

Fig. 12. Equivalent porosity of different ITZs and adjacent matrix.

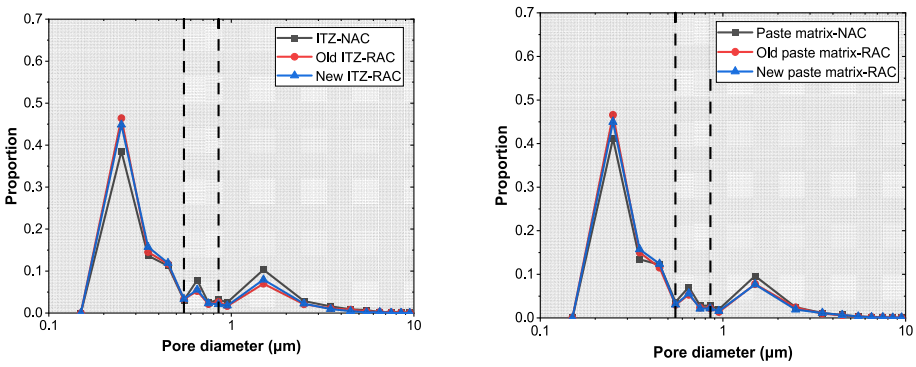

(a) ITZs (b) Paste matrix

Fig. 13. Equivalent pore diameter distribution of different ITZs and adjacent matrix.
Note: According to the pore size, the area divided by the dash lines from left to right is slight defects, moderate defects and severe defects, respectively.

Table 5
Contents of pores and cracks, unreacted products and reaction products within ITZs and adjacent paste matrix.

Regions	Constituents proportion		
	Pores and Cracks	Unreacted products	Reaction products
ITZ-NAC	10.52 % ± 5.77 %	13.37 % ± 3.30 %	76.12 % ± 2.54 %
Paste matrix-NAC	5.77 % ± 0.75 %	17.94 % ± 1.57 %	76.29 % ± 2.22 %
Old ITZ-RAC	11.58 % ± 4.16 %	11.90 % ± 3.01 %	76.51 % ± 1.54 %
Old paste matrix-RAC	7.60 % ± 1.36 %	12.49 % ± 0.89 %	79.91 % ± 1.87 %
New ITZ-RAC	8.69 % ± 0.36 %	12.95 % ± 1.92 %	78.36 % ± 1.89 %
New paste matrix-RAC	6.98 % ± 0.69 %	16.50 % ± 1.86 %	76.52 % ± 1.99 %

the average volume fraction of pores and cracks in Paste matrix-NAC was 1.21 % lower than that in New paste matrix-RAC. The average volume fractions of pore and cracks in the old ITZ and old paste matrix in RAC were the highest, which were 11.58 % and 7.6 %, respectively. This is mainly related to the water-cement ratio of the old mortar and the cracks created in the old mortar during the crushing process. For unreacted products, the proportion in the ITZ was consistently lower compared to paste matrix. Among them, the old cement pastes in RAC had the lowest difference because of the longer curing age. The reaction product content in ITZ was always lower than paste matrix, but in the new cement paste of RAC, the reaction product volume fraction of new ITZ reached 78.36 %, which was higher than 76.52 % in new paste matrix. A small amount of incompletely hydrated cement clinkers in the old paste matrix secondary hydrated during the curing process, which promoted the hydration degree in the New ITZ-RAC.

(a) NAC-0 (b) NAC-3 (c) NAC-7 (d) NAC-14 (e) NAC-14-5 (f) NAC-14-9 (g) NAC-14-13

(h) RAC50-0 (i) RAC50-7 (g) RAC50-14 (k) RAC50-14-5 (l) RAC50-14-13 (m) RAC100-0 (o) RAC100-3

(p) RAC100-7 (q) RAC100-14 (r) RAC100-14-5 (s) RAC100-14-9 (t) RAC100-14-13

Fig. 14. Failure modes of RAC under triaxial compression and pore water pressure.

3.4. Failure modes of RAC under confining pressure and pore water pressure

The failure modes of concrete specimens under various stress states are shown in Fig. 14. The RCA replacement ratio had no significant effect on the failure patterns of the specimens. Under uniaxial compression, NAC-0 and RAC50-0 and RAC100-0 were damaged most severely. Multiple longitudinal main cracks appeared on the surface of the concrete specimen, showing a radial splitting failure mode. For the concrete specimens damaged by triaxial compression, the damage severity was obviously alleviated. The longitudinal crack with branches was replaced by an oblique crack. At this time, the concrete specimen presented a shear failure mode, which is consistent with existing knowledge [51,52]. Under the confining pressure combined with pore water pressure condition, the damage degree of concrete specimens was further reduced when the target radial strain was reached. At this time, there were no obvious main cracks on the surface of three groups of concrete, because the internal friction between cement particles was weakened by pore water, and many fine cracks appeared on the concrete surface.

3.5. Stress-strain curves analysis

The measured stress-strain curves of NAC and RAC under different stress states are shown in Fig. 15. The corresponding stress parameters, peak strength, axial peak strain, radial peak strain, maximum volumetric strain and elastic modulus are given in Table 6. The elastic modulus was obtained according to ASTM C469 as follows:

$$E = \frac{40\%f_c - \sigma_1(0.005\%)}{\varepsilon_1(40\%f_c) - 0.005\%} \tag{4}$$

where σ_1 (0.005 %) and ε_1 (40%f_c) represent the axial stress when the axial strain is 0.005 % and the axial strain when the axial stress reaches 40%f_c, respectively.

3.5.1. Influence of confining pressure on the stress-strain curves

It is easy to be conscious of the contribution of lateral confinement to the compressive strength and ductility of concrete samples from stress-strain curves in Fig. 15. Under uniaxial compression, the concrete specimen quickly entered the descending section after reaching the peak stress. During the entire compression process, the axial deformation of the specimens was small, while after fully failure, the radial strain increased rapidly as the stress decreased due to the lack of lateral confinement. In comparison, the triaxial compression strength of concrete specimens increased significantly compared to uniaxial compression. For example, Fig. 15 (a) shows that the compressive strength of the NAC specimen improved from 29.36 MPa under uniaxial compression to 124.31 MPa when the confining pressure was 14 MPa. This phenomenon can be attributed to the fact that the lateral positive confinement restrained the lateral deformation and crack propagation. In addition, lateral pressure enhanced the internal friction between the coarse aggregate, fine aggregate and C-S-H gel, which improved the external force required for the shear-slip failure of the specimens.

It can also be seen from the rising section of the stress-strain curve that after the initial linear growth, the stress rising rate of the concrete specimens under triaxial compression gradually slowed down with the strain, and this plasticity stage become more apparent with the increase of confining pressure. Correspondingly, the peak axial strain of concrete specimens increased with the confining pressure. For NAC, it increased from 0.101 % under uniaxial compression to 0.973 % when the confining pressure was 14 MPa. After passing the peak point, unlike the uniaxial compression, the stress-strain curve of concrete specimens under high confining pressure had a gentler descending section, showing an obvious plastic failure characteristic. However, compared with the axial stress and axial deformation, the variation law of the radial peak strain and elastic modulus of concrete specimens with confining pressure was not obvious. Similar observations were also found in the studies of Chen et al. [27] and Folino et al. [26]. This may be attributed to the combined effect of lateral confinement and plasticization of concrete

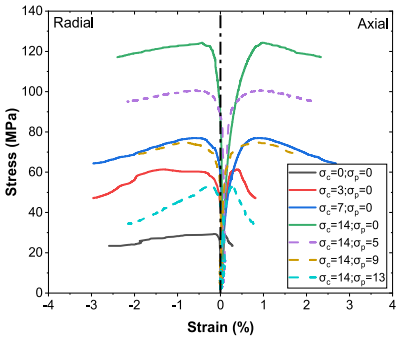

(a) NAC

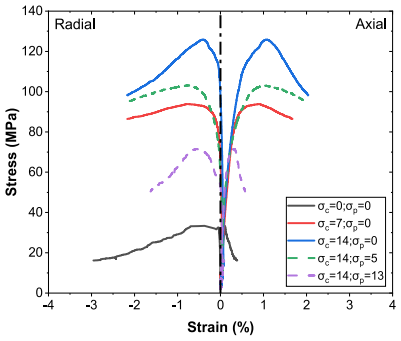

(b) RAC50

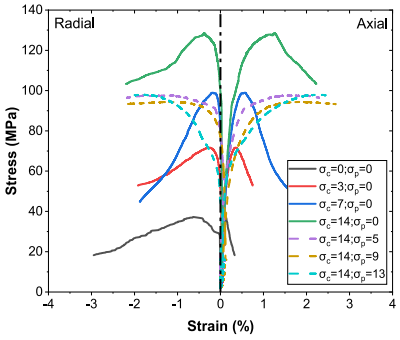

(c) RAC100

Fig. 15. Stress-strain curves of concrete samples under triaxial compression.

Table 6
Mechanical properties of NAC and RAC obtained from stress-strain curves.

Specimens	σ_c (MPa)	σ_p (MPa)	f_c (MPa)	S.D.	ε_{3p} (%)	ε_{1p} or ε_{2p} (%)	ε_{vp} (%)	E (GPa)	S.D.
NAC-0	0	0	29.36	1.66	0.101	−0.159	0.0485	30.35	1.36
NAC-3	3	0	61.38	1.93	0.381	−0.466	0.1285	35.71	1.24
NAC-7	7	0	76.99	2.31	0.911	−0.611	0.2794	35.51	2.21
NAC-14	14	0	124.31	1.34	0.973	−0.430	0.3982	42.10	1.07
NAC-14-5	14	5	100.79	1.68	0.924	−0.559	0.2784	53.09	3.03
NAC-14-9	14	9	74.98	3.21	0.784	−0.789	0.0642	60.54	2.15
NAC-14-13	14	13	52.9	1.12	0.273	−0.248	0.2168	67.82	1.69
RAC50-0	0	0	33.35	2.58	0.099	−0.372	0.0252	40.59	2.16
RAC50-7	7	0	93.81	1.62	0.899	−0.768	0.2118	30.96	3.56
RAC50-14	14	0	125.87	2.06	1.070	−0.411	0.4781	38.72	2.45
RAC50-14-5	14	5	103.1	1.24	0.998	−0.744	0.1551	52.93	2.36
RAC50-14-13	14	13	71.5	2.33	0.312	−0.551	0.1214	65.68	1.87
RAC100-0	0	0	37.26	2.15	0.120	−0.638	0.0365	42.51	1.69
RAC100-3	3	0	71.68	1.98	0.348	−0.259	0.1282	48.61	2.15
RAC100-7	7	0	98.95	2.13	0.569	−0.188	0.2934	40.90	1.57
RAC100-14	14	0	128.42	1.19	1.263	−0.130	0.4541	45.69	2.36
RAC100-14-5	14	5	97.7	0.96	1.472	−1.104	0.3227	41.97	3.14
RAC100-14-9	14	9	94.44	1.25	1.841	−1.213	0.51	28.84	3.41
RAC100-14-13	14	13	98.03	2.16	2.23	−1.784	0.1373	61.48	2.21

Note: σ_c represents confining pressure; σ_p represents pore water pressure; f_c represents compressive strength; ε_{3p} represents axial peak strain; ε_{1p} and ε_{2p} represent radial peak strain; ε_{vm} represents the maximum volumetric strain; E represents elastic modulus; S.D. represents standard deviation.

specimens under high confining pressure.

3.5.2. Influence of RCA replacement ratio and ITZs on the stress-strain curves

The uniaxial compressive strength of RAC50 and RAC100 were 33.35 MPa and 33.76 MPa, respectively, which were higher than that of NAC. This trend continued to triaxial compression (125.87 MPa for RAC50-14 and 128.42 MPa for RAC100-14 vs. 124.31 MPa for NAC-14). According to Vargas et al. [53], when concrete specimens is under compression, ITZ often experiences stress concentration, which determines the compressive strength of concrete. However, the nanoindentation test results in Table 4 show that the micromechanical properties of the old and new ITZs and adjacent cement paste of RAC were higher than those of the corresponding regions in NAC. In addition, by comparing the porosity in Table 5, the porosity of the old ITZ-RAC was similar to that of ITZ-NAC, while the porosity of the new ITZ-RAC was lower than that of ITZ-NAC. Obviously, RAC was better than NAC regardless of the analysis from macromechanical properties, micromechanical properties and microstructure levels, which is inconsistent with previous knowledge [54]. It is worth noting that the curing age of concrete specimens in this study was relatively long (about one year). Therefore, we can conclude that RAC can achieve satisfactory mechanical properties after a long-term curing.

For the stress-strain curves of the RAC, another noteworthy difference from the NAC occurred in the descending section. The descending sections of the stress-strain curves for RAC50-14, RAC100-7 and RAC100-14 are steeper than the descending sections of NAC at the same stress states. From the nanoindentation test results from Table 4, ITZ-RAC and Paste matrix-RAC showed better micromechanical properties than ITZ-NAC and Paste matrix-NAC. Therefore, RAC showed more brittle damage characteristics under triaxial compression, although the lateral confinement increased its plastic deformation capacity compared to uniaxial compression.

3.5.3. Influence of pore water pressure and ITZs on the stress-strain curves

Similar to the confining pressure, the pore water pressure can also significantly change the concrete triaxial compressive stress-strain trend. For NAC and RAC50, the peak stress and axial peak strain of specimens gradually decreased, whereas the elastic modulus increased with pore water pressure as shown in Fig. 15 (a) and (b). As explained earlier, pore water weakened the internal friction that contributed prominently to concrete triaxial compressive strength. The slip between the failure surface was easier by the lubricating effect of pore water. In addition, the infiltration of pore water under compression contributed more to the propagation of initial microcracks, resulting in a decrease in compressive strength. RAC100 is different from NAC and RAC50. Under 5 MPa pore water pressure, the triaxial compressive strength of RAC100 decreased to around 98 MPa and maintained at this value when the pore water pressure improved to 9 MPa and 13 MPa as shown in Fig. 15 (c). However, the axial peak strain increased with pore water pressure. This stress-strain form is similar to the changing pattern of stress-strain curves of concrete with different saturations under high confining pressure by Vu and Malecot et al. [33,34]. It can be seen that pore water pressure had a great influence on the ultimate stress of low strength concrete. For RAC100, the micromechanical properties of old and new ITZs and paste matrix were better than those corresponding regions within NAC. Moreover, RAC had less severe defects which reduce mechanical properties. During compression, the supporting effect of pore water pressure became more pronounced, improving the axial peak strain of RAC before destruction.

3.5.4. Detailed mechanical properties analysis

In order to further compared the influence of confining pressure and pore water pressure on the mechanical properties of NAC and RAC, peak stress, peak strain and elastic modulus were normalised. The corresponding data are shown in Fig. 16. It can be seen from Fig. 16 (a) that as the confining pressure increased, the normalised axial stress increased gradually, and the improving rate of NAC and RAC was similar. However, when pore water pressure existed, the normalised axial stress of NAC decreased gradually with pore water pressure. The normalised axial stress of RAC50 also showed a decreasing trend with pore water pressure, but the descending rate was slightly lower than that of NAC, because NAC had higher severe defects (see Fig. 13). For RAC100, when it suffered pore water pressure, the normalised axial stress dropped rapidly from 3.45, without pore water pressure, to 2.62, and no longer changed significantly with the increase of pore water pressure. This is because RAC possessed better micromechanical properties and microstructure performance according to data in Section 3.2 and 3.3. In this condition, the supporting effect of pore water was more prominent, but the promoting effect on cracks expansion was not obvious.

As shown in Fig. 16 (b), due to the positive lateral confinement, the normalised axial strain of NAC and RAC50 increased gradually with the confining pressure, while the pore water pressure accelerated the expansion of microcracks, so that the normalised axial strain gradually decreased. It should be noted that due to better micromechanical properties of RAC100, the supporting effect of pore water pressure was

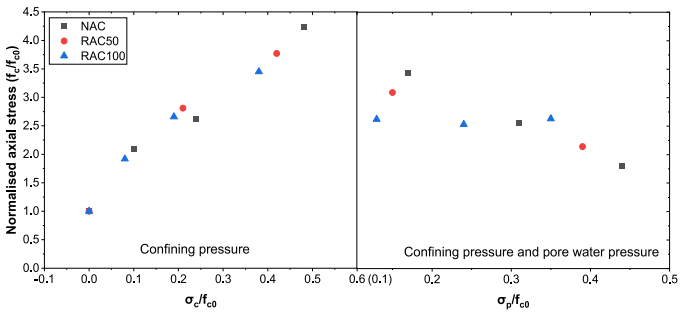

(a) Contribution of confining pressure and pore water pressure to peak stress

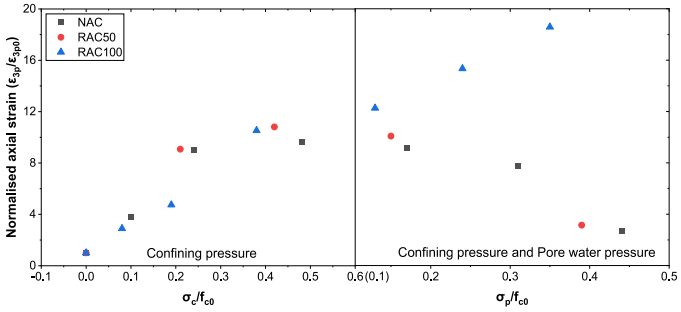

(b) Contribution of confining pressure and pore water pressure to axial strain

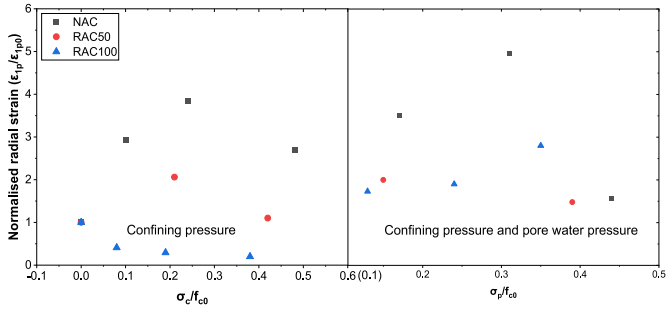

(c) Contribution of confining pressure and pore water pressure to radial strain

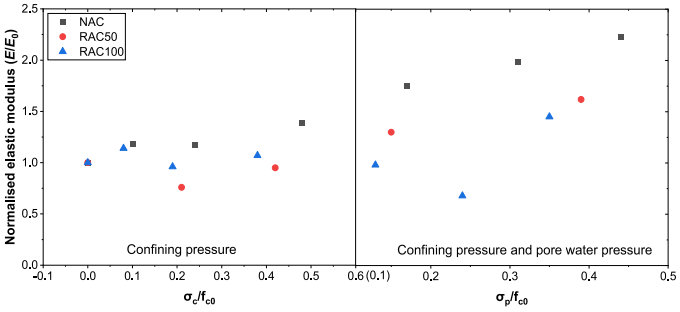

(d) Contribution of confining pressure and pore water pressure to elastic modulus

Fig. 16. Limit state of RAC under triaxial compression and pore water pressure.

more obvious, which improved the normalised axial peak strain to 18.58 under the 14 MPa confining pressure and 13 MPa pore water pressure. In contrast, the variation law of normalised radial strain under different confining pressure and pore water pressure was not clear in Fig. 16 (c). Only RAC100 showed an increasing trend in the normalised radial strain when the pore water pressure existed. The normalised elastic modulus did not vary obviously under different confining pressure, and the values of the three types of concrete were ranged between 0.7 and 1.4, as

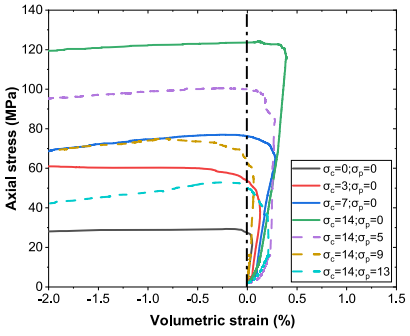

(a) NAC

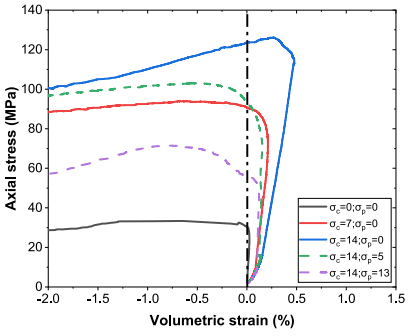

(b) RAC50

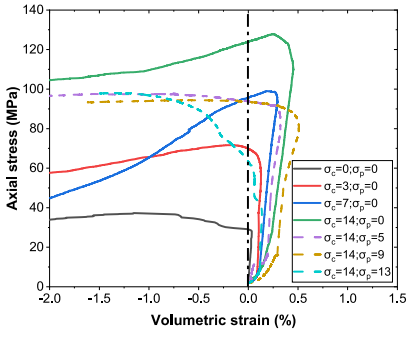

(c) RAC100

Fig. 17. Axial stress-volumetric strain curves of concrete samples under triaxial compression.

shown in Fig. 16 (d). However, with the increase of pore water pressure, the normalised elastic modulus of concrete specimens increased gradually except for RAC100-14-9. As explained earlier, the pore water pressure enhanced the initial stiffness of concrete specimens under compression.

3.6. Axial stress-volumetric strain analysis

The volumetric strain of concrete specimens can be calculated according to the equation $\varepsilon_v = \varepsilon_1 + \varepsilon_2 + \varepsilon_3$. The relationship curves of volumetric strain and axial stress of NAC and RAC under different stress states are shown in Fig. 17. The maximum volumetric strains of both NAC and RAC gradually increased with confining pressure, mainly because the lateral confinement enhanced the plastic deformation ability of concrete before failure. However, when a 13 MPa pore pressure existed, the maximum volumetric strain of NAC, RAC50 and RAC100 decreased from 0.3982 %, 0.4781 % and 0.4541 %, without pore water pressure, to 0.2168 %, 0.1214 % and 0.1373 %, respectively.

The contribution of confining pressure and pore water pressure to the normalised maximum volumetric strain is shown in Fig. 18. It can be clearly seen that with the increase of confining pressure, the normalised volumetric strain increased gradually, while the growth rate of NAC was slower. When subjected to pore water pressure, the normalised volumetric strain decreased to 4–8 compared to uniaxial compression, except for RAC100-14-9 ($\sigma_p/f_{c0} = 0.24$).

4. Failure criteria

4.1. Triaxial compression

4.1.1. Mohr-Coulomb failure criterion

The Mohr-Coulomb failure criterion has been widely used to describe the failure surface of concrete under triaxial compression. It assumes that the triaxial compressive strength of concrete has a linear relationship with the confining pressure. The expression is as follows [55]:

$$\frac{f_c}{f_{c0}} = k\frac{\sigma_c}{f_{c0}} + 1 \tag{5}$$

where, f_c and f_{c0} are the triaxial compressive strength and uniaxial compressive strength of concrete, respectively. σ_c is the confining pressure. k is a parameter related to the internal friction angle, which needs to be obtained by regression analysis on experimental data. According to Li et al. [55], recycled aggregate would not affect the internal frication angle of concrete under triaxial compression. Therefore, the relationship between the triaxial compressive strength and confining pressure of NAC and RAC can be expressed by the same linear equation:

$$\frac{f_c}{f_{c0}} = 6.96\frac{\sigma_c}{f_{c0}} + 1 \tag{6}$$

The experimental data and fitting curve are shown in Fig. 19. The triaxial compressive strength and confining pressure of NAC and RAC showed a strong linear relationship ($R^2 = 0.953$).

4.1.2. William-Warnke failure criterion

The William-Warnke failure criterion is another three-parameter model. It can be used to describe the relationship between the principal shear stress and mean principle stress of concrete in triaxial compression as shown in Eqs. (7)–(9) [31].

$$\frac{\tau_m}{f_{c0}} = a_1 + b_1\left(\frac{\sigma_m}{f_{c0}}\right) - c_1\left(\frac{\sigma_m}{f_{c0}}\right)^2 \tag{7}$$

$$\sigma_m = \frac{1}{3}(\sigma_1 + \sigma_2 + \sigma_3) \tag{8}$$

$$\tau_m = \frac{1}{\sqrt{15}}\sqrt{(\sigma_1 - \sigma_2)^2 + (\sigma_1 - \sigma_3)^2 + (\sigma_2 - \sigma_3)^2} \tag{9}$$

where τ_m and σ_m represent the principal shear stress and mean principal stress of concrete specimens, respectively. a_1, b_1 and c_1 are the corresponding parameters. Through the regression analysis of the experimental data in the present study, the expression of the William-Warnke

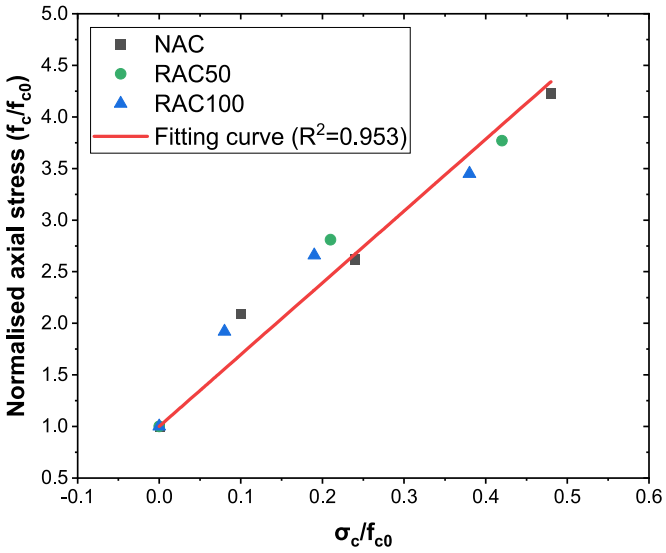

Fig. 19. Mohr-Coulomb failure criteria for RAC under triaxial compression.

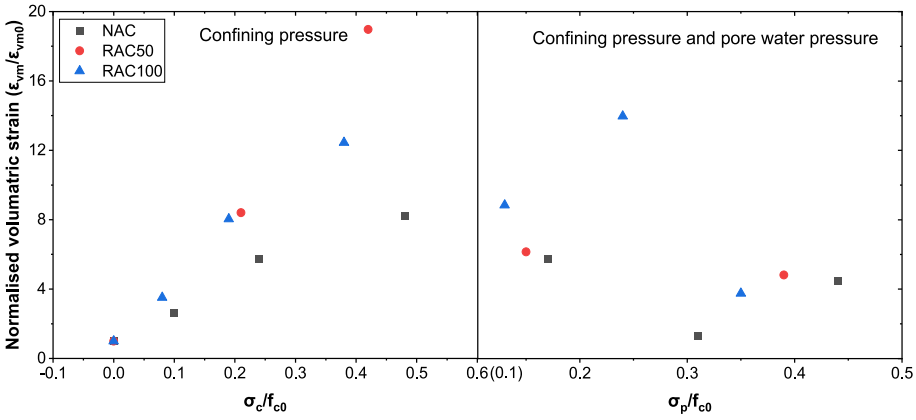

Fig. 18. Limit volumetric strain of RAC under triaxial compression and pore water pressure.

failure criterion of NAC and RAC can be written as Eq. (10).

$$\frac{\tau_m}{f_{c0}} = -0.045 + 0.806\left(\frac{\sigma_m}{f_{c0}}\right) + 0.109\left(\frac{\sigma_m}{f_{c0}}\right)^2 \tag{10}$$

The testing data and the fitting curve are shown in Fig. 20. It can be seen that the fitting performance of the William-Warnke failure criterion can achieve a better fitting results than Mohr-Coulomb failure criterion. The rising rate of principal shear stress of NAC with confining pressure is close to that of RAC50 and RAC100.

4.1.3. Power-Law failure criterion

The Power-Law failure criterion is a two-parameter exponential model as shown in Eq. (11) [56].

$$\frac{f_c}{f_{c0}} = a_2\left(\frac{\sigma_c}{f_{c0}}\right)^{b_2} + 1 \tag{11}$$

where, a_2 and b_2 are parameters, which are calculated to be 5.13 and 0.70 respectively through the experimental data. Therefore, the Power-Law failure criterion equation of NAC and RAC can be written as:

$$\frac{f_c}{f_{c0}} = 5.13\left(\frac{\sigma_c}{f_{c0}}\right)^{0.7} + 1 \tag{12}$$

It can be seen from Fig. 21 that the Power-Law failure criterion can achieve a satisfying fitting performance ($R^2 = 0.989$) on the limit states of NAC and RAC under triaxial compression, which is consistent with the conclusion of Wu et al. [31].

4.2. Triaxial compression with pore water pressure

At present, there are few failure criterion theoretical models suitable for analysing the coupling effect of confining pressure and pore water pressure on RAC. Based on experimental data, as shown in Fig. 16 (a), it can be roughly concluded that the triaxial compressive strength of NAC and RAC50 under the 14 MPa confining pressure decreased linearly with the increase of pore water pressure. Therefore, we assume that the triaxial compressive strength and pore water pressure of NAC and RAC50 have the following relationship:

$$f_c = k_2\sigma_p + f_{c14} \tag{13}$$

where, f_c and f_{c14} are the triaxial compressive strength and triaxial compressive strength with a confining pressure of 14 MPa, respectively. σ_p is the pore water pressure. The fitting curves of NAC and RAC50 can

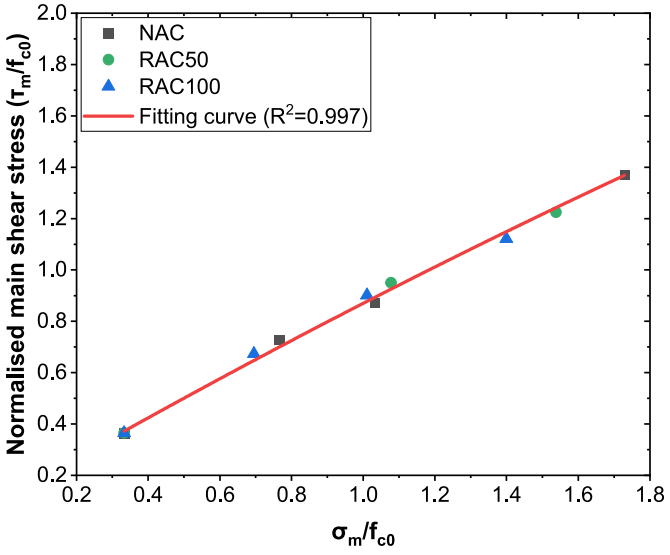

Fig. 20. William-Warnke failure criteria for RAC under triaxial compression.

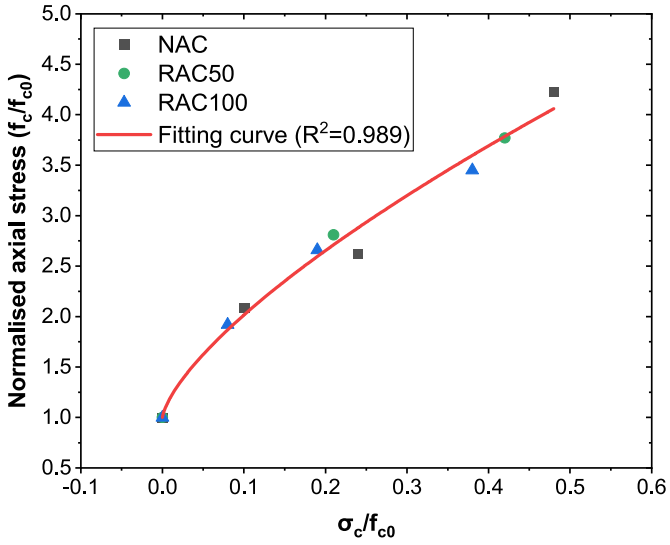

Fig. 21. Power-Law failure criteria for RAC under triaxial compression.

be obtained from the experimental data as Eqs. (14) and (15).

$$\mathrm{NAC}f_c(NAC) = -5.42\sigma_p + f_{c14}(NAC) \tag{14}$$

$$\mathrm{RAC50}f_c(RAC50) = -4.23\sigma_p + f_{c14}(RAC50) \tag{15}$$

For RAC100, we can refer to the theoretical model Eq. (16) proposed by Malecot et al. [34].

$$\sigma_{c-sat} = \sigma_{cp0} - \lambda\varphi_{air}^{1/3} - \kappa\varphi_{cap}^{1/3} \tag{16}$$

where, $\sigma_{c\text{-}sat}$ and σ_{cp0} are the triaxial compressive strength of saturated concrete specimen and dry concrete specimen, respectively. Φ_{air} and Φ_{cap} are entrained air porosity and capillary porosity, respectively. λ and κ are parameters.

In concrete, ITZs accounts for about 20%–30 % of the total volume of cement paste [57]. Here, we take 25 %. RAC100 possesses two kinds of ITZs as old ITZ and new ITZ, which are assumed to account for 50 % of the total cement paste volume. According to Jayasuriya et al. [58], the ratio of old mortar to new mortar is assumed to be 1:9. Combined with the micromechanical test data in this study, Eq. (16) is modified to the following Eq. (17) considering ITZ porosity and mortar porosity.

$$f_c(RAC100) = f_{c14}(RAC100) - \alpha(\varphi_{old\ ITZ} + \varphi_{new\ ITZ})\times 0.5 - \beta\left(\frac{1}{10}\varphi_{old\ mortar} + \frac{9}{10}\varphi_{new\ mortar}\right)\times 0.5 \tag{17}$$

where, $\varphi_{old\ ITZ}$ and $\varphi_{new\ ITZ}$ are the porosity of old and new ITZ in RAC, respectively. $\varphi_{old\ mortar}$ and $\varphi_{new\ mortar}$ are the porosity of old and new mortar in RAC respectively. α and β are the parameters, which were calibrated as 210 and 235 respectively. The experimental data and fitting curves of three groups of concrete specimens are shown in Fig. 22.

5. Stress-strain model

5.1. Uniaxial compression

The stress-strain curves of NAC and RAC under uniaxial compression can be simply divided into ascending and descending sections. Tang et al. [13] made a comprehensive comparison of the existing stress-strain empirical models of RAC specimens under uniaxial compression, and concluded that the model proposed by Collins and Mitchell [59] is close to the experimental data. The experimental model can be express as:

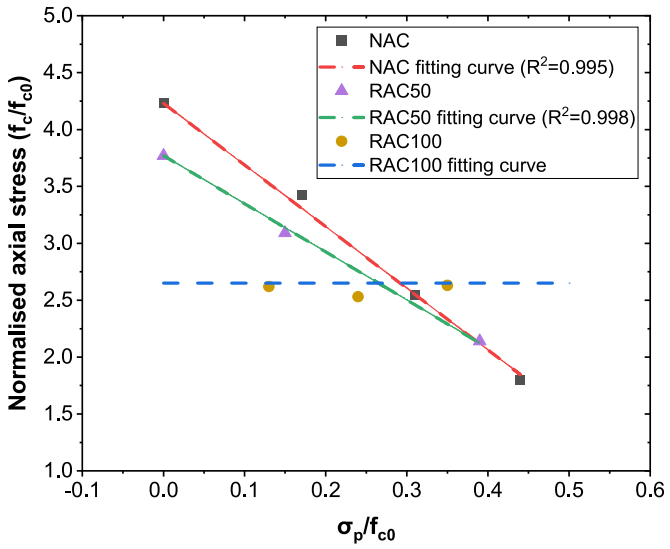

Fig. 22. Failure criteria for RAC under triaxial compression with pore water pressure.

$$\frac{\sigma_3}{f_{c0}}=\begin{cases}\dfrac{A_1\left(\dfrac{\varepsilon_3}{\varepsilon_{3p0}}\right)}{A_1-1+\left(\dfrac{\varepsilon_3}{\varepsilon_{3p0}}\right)^{A_1}} & 0\le\dfrac{\varepsilon_3}{\varepsilon_{3p0}}<1\\ \dfrac{A_1\left(\dfrac{\varepsilon_3}{\varepsilon_{3p0}}\right)}{A_1-1+\left(\dfrac{\varepsilon_3}{\varepsilon_{3p0}}\right)^{A_1B_1}} & \dfrac{\varepsilon_3}{\varepsilon_{3p0}}\ge 1\end{cases} \tag{18}$$

Therefore, this study corrected the parameters of Collins and Mitchell model to predict the NAC and RAC uniaxial compression experimental data in Fig. 15. For NAC, RAC50 and RAC100, parameter A_1 is 2.89, and parameter B_1 is 0.84. The fitting results are shown in Fig. 23. It can be seen that the modified Collins and Mitchell model slightly underestimates the stress of the later decline section of NAC. A satisfactory fitting performance are achieved for the other sections and curves.

5.2. Triaxial compression

For the stress-strain curves of NAC and RAC under triaxial compression, the model Eq. (19) proposed by Guo and Zhang [60] was selected.

$$\frac{\sigma_3}{f_c}=\begin{cases}\dfrac{A_2\left(\dfrac{\varepsilon_3}{\varepsilon_{3p}}\right)+(3-2A_2)\left(\dfrac{\varepsilon_3}{\varepsilon_{3p}}\right)^2+(A_2-2)\left(\dfrac{\varepsilon_3}{\varepsilon_{3p}}\right)^3}{B_2\left(\dfrac{\varepsilon_3}{\varepsilon_{3p}}-1\right)^2+\left(\dfrac{\varepsilon_3}{\varepsilon_{3p}}\right)} & 0\le\dfrac{\varepsilon_3}{\varepsilon_{3p}}<1\end{cases} \tag{19}$$

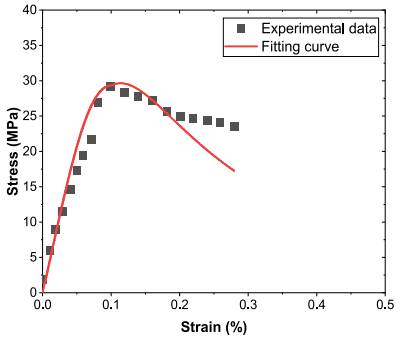

(a) NAC-0

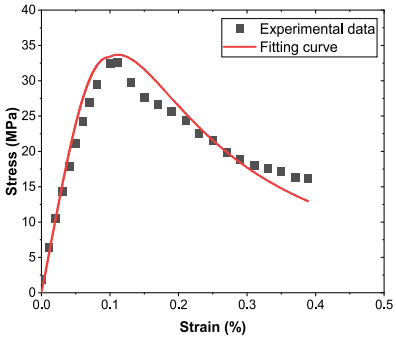

(b) RAC50-0

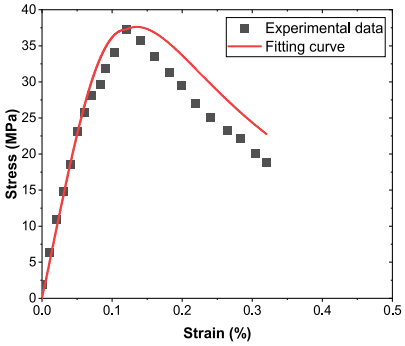

(c) RAC100-0

Fig. 23. Stress-strain fitting curves of NAC and RAC under uniaxial compression.

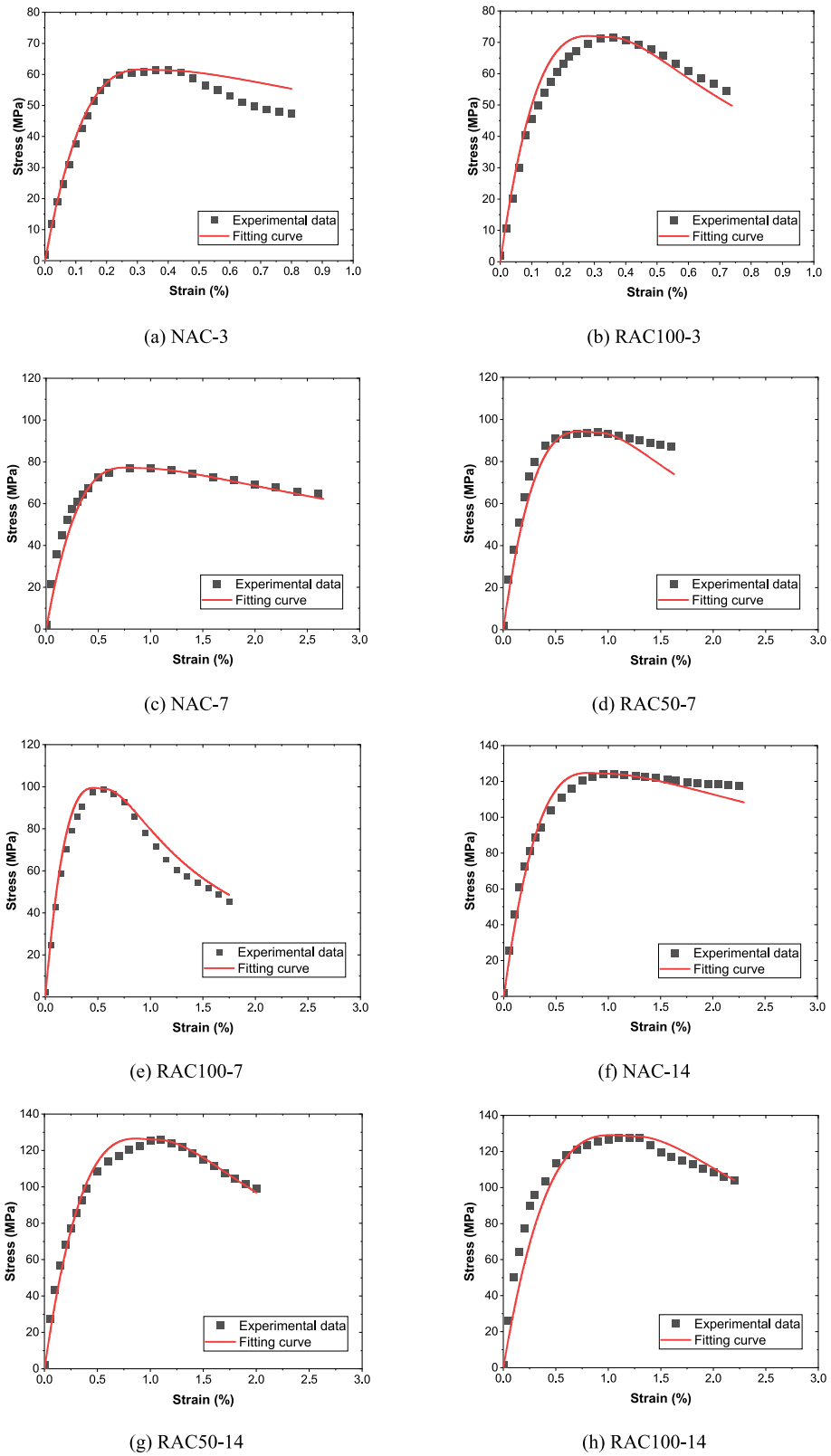

Fig. 24. Stress-strain fitting curves of NAC and RAC under triaxial compression.

$$\frac{\varepsilon_3}{\varepsilon_{3p}} \geq 1$$

The parameters were determined by regression analysis, in which A_2 and B_2 for NAC were 3.36 and 0.19; A_2 and B_2 for RAC50 and RAC100 were 3.41 and 0.74, respectively. The fitting results are shown in Fig. 24. It can be seen that, there is a certain difference between the fitting results and test data in the descending sections of NAC-3, NAC-14 and RAC50-7. However, the fitting results of rest curves have a satisfying degree of agreement.

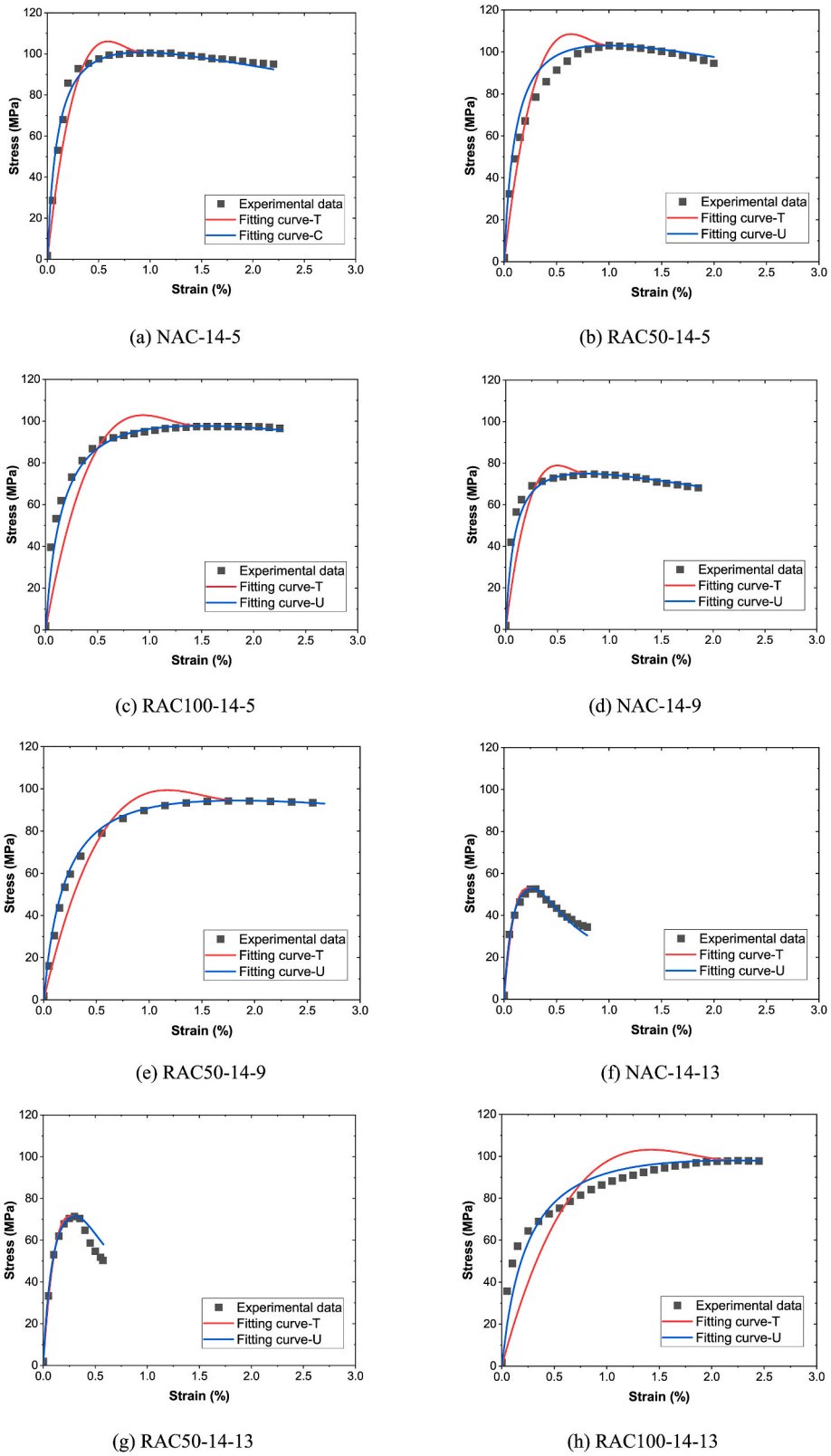

Fig. 25. Stress-strain fitting curves of NAC and RAC under triaxial compression with pore water pressure.

5.3. *Triaxial compression with pore water pressure*

It has been known in the analysis of the stress-strain curves in Fig. 15 that the pore water pressure reduced the compressive strength of the concrete specimens under a fixed confining pressure and improved the elastic modulus. This characteristic is also reflected in the fitting analysis of stress-strain curves. As shown in Fig. 25, the triaxial compressive stress-strain model Eq. (19) (fitting curve-T in Fig. 25) overestimates the compressive strength and underestimates the elastic modulus when concrete specimens were subjected to pore water pressure. Chen et al.

[27] proposed a new empirical model, which was originally developed from Euro Code CEB-FIP [61] and Guo and Zhang [60] model to predict the RAC stress-strain relationship. The Chen's model can be expressed as:

$$\frac{\sigma_3}{f_c}=\begin{cases}\dfrac{A_3\left(\dfrac{\varepsilon_3}{\varepsilon_{3p}}\right)-\left(\dfrac{\varepsilon_3}{\varepsilon_{3p}}\right)^2}{1+(A_3-2)\left(\dfrac{\varepsilon_3}{\varepsilon_{3p}}\right)} & 0\le\dfrac{\varepsilon_3}{\varepsilon_{3p}}<1\\ \dfrac{\dfrac{\varepsilon_3}{\varepsilon_{3p}}}{B_2\left(\dfrac{\varepsilon_3}{\varepsilon_{3p}}-1\right)^2+\left(\dfrac{\varepsilon_3}{\varepsilon_{3p}}\right)} & \dfrac{\varepsilon_3}{\varepsilon_{3p}}\ge 1\end{cases} \tag{20}$$

It can be seen that the stress-strain model Eq. (20) (Fitting curve-C in Fig. 25) has a better fitting performance on peak stress and slop of ascending sections. In Eq. (20), for NAC-14-5, NAC-14-9, RAC50-14-5, RAC100-14-5, RAC100-14-9, RAC100-14-13, the parameters A_3 and B_3 are 10.629 and 0.112. For NAC-14-13 and RAC50-14-13, the descending section of stress-strain curves are steeper. As a result, the parameters A_3 and B_3 are 3.254 and 0.592.

6. Conclusions

In this paper, concretes with different RCA replacement ratios of 0 %, 50 % and 100 % were prepared. The BSE-image analysis technique and nanoindentation were used to determine the width of the ITZs and compare the constituent composition and micromechanical properties of the ITZs and the adjacent paste matrix. Then, NAC and RAC specimens were subjected to confining pressure ranging from 0 to 14 MPa and pore water pressure from 0 to 13 MPa. Stress-strain curves were obtained under these various stress conditions. The following conclusions can be drawn:

(1) The micromechanical properties of ITZ are related to the characteristics of contact surface. Due to the rough surface of the old mortar and one year of continuous secondary hydration, the elastic modulus of New ITZ-RAC was 9.51 GPa, higher than that of ITZ-NAC with the same water-cement ratio. The micromechanical properties of adjacent paste matrix were less affected by the characteristics of contact surface, but the elastic modulus of New paste matrix-RAC was still 7.8 GPa higher than that of Paste matrix-NAC. The elastic modulus of Old ITZ-RAC was close to that of ITZ-NAC, about 14.44 GPa.

(2) Compared with New ITZ-RAC, ITZ-NAC had fewer small pores from 0.2 to 0.3 μm and more large pores from 1 to 2 μm. The porosities of ITZ-NAC and Old ITZ-RAC were similar (10.52 % and 11.58 %, respectively), whereas the porosity of New ITZ-RAC in contact with old mortar was lower (8.69 %).

(3) The compressive strength, axial peak strain and maximum volumetric strain of NAC and RAC increased gradually with the increase of confining pressure. The failure pattern converted from radial splitting failure mode under uniaxial compression to shear-slip failure mode. Due to the higher elastic modulus and hardness of New ITZ-RAC and New paste matrix-RAC, RAC exhibited higher post-peak brittle failure characteristics. The variation law of elastic modulus and radial peak strain of concrete specimens with confining pressure was not obvious.

(4) When subjected to pore water pressure, NAC and RAC had decreased compressive strength and maximum volumetric strain but increased elastic modulus with pore water pressure. For RAC100 with higher micromechanical properties, the supporting effect of pore water was more prominent. As a result, the axial peak strain of RAC100 increased with pore water pressure. However, NAC and RAC50 showed the adverse trend.

(5) Willam-Warnke failure criterion can well describe the relationship between principal normal stress and principal shear stress of NAC and RAC. The relationship between the peak stress and pore water pressure of NAC and RAC50 can be described by linear descending functions. However, the normalised axial stress of RAC100 dropped to about 2.6 and did not change obviously with pore water pressure. Its value can be described by the modified equation proposed by Malecot et al. [30].

(6) The stress-strain model can well predict the stress-strain curves of NAC and RAC under uniaxial and triaxial compression. However, the triaxial compression model overestimated the peak stress and underestimated the elastic modulus when subjected to pore water pressure. In contrast, the modified Chen's model [24] can achieve a satisfactory fitting performance for the coupling state of confining pressure and pore water pressure.

(7) Pore water pressure plays an important role in the triaxial compression behaviour of RAC. This study conducted triaxial compression experiments on RAC at constant pore water pressure of 5–13 MPa. However, the number of concrete specimens for mechanical properties analysis under multi-field loads is limit. In the future, mechanical properties tests of RAC over wider confining pressure and pore water pressure range can be designed. In addition, durability investigation such as permeability and creep tests under complicated stress states can be considered.

Declaration of competing interest

The authors declare that they have no known competing financial interests or personal relationships that could have appeared to influence the work reported in this paper.

Data availability

Data will be made available on request.

Acknowledgements

The authors would like to appreciate the support from Australian Research Council (ARC), Australia (FT220100177, LP230100288, DP220101051, DP220100036, IH200100010).

References

[1] S. Zhang, R. Liu, C. Lu, Y. Gao, J. Xu, L. Yao, Y. Chen, Application of digital image correlation to study the influence of the water/cement ratio on the interfacial transition zone in cement-based materials, Construct. Build. Mater. 367 (2023), 130167.
[2] G. Yue, Z. Ma, M. Liu, C. Liang, G. Ba, Damage behavior of the multiple ITZs in recycled aggregate concrete subjected to aggressive ion environment, Construct. Build. Mater. 245 (2020), 118419.
[3] P.R. Rangaraju, J. Olek, S. Diamond, An investigation into the influence of inter-aggregate spacing and the extent of the ITZ on properties of Portland cement concretes, Cement Concr. Res. 40 (2010) 1601–1608.
[4] A. Djerbi, Effect of recycled coarse aggregate on the new interfacial transition zone concrete, Construct. Build. Mater. 190 (2018) 1023–1033.
[5] Z. Luo, W. Li, K. Wang, S.P. Shah, Research progress in advanced nanomechanical characterization of cementbased materials, Cem. Concr. Compos. 94 (2018) 277–295.
[6] K. Lyu, W. She, H. Chang, Y. Gu, Effect of fine aggregate size on the overlapping of interfacial transition zone (ITZ) in mortars, Construct. Build. Mater. 248 (2020), 118559.
[7] M. Nuruzzaman, P.K. Sarker, F.U.A. Shaikh, The interfacial transition zone microstructure of ground ferronickel slag incorporated self-compacting concrete investigated by nanoindentation, J. Build. Eng. 71 (2023), 106437.
[8] A. Hosan, F.U.A. Shaikh, P. Sarker, F. Aslani, Nano- and micro-scale characterisation of interfacial transition zone (ITZ) of high volume slag and slag-fly ash blended concretes containing nano SiO2 and nano CaCO3, Construct. Build. Mater. 269 (2021), 121311.

[9] I.F.S.d. Bosque, W. Zhu, T. Howind, A. Matías, M.I.S.d. Rojas, C. Medina, Properties of interfacial transition zones (ITZs) in concrete containing recycled mixed aggregate, Cem. Concr. Compos. 81 (2017) 25–34.
[10] Y. Wei, W. Kong, Y. Wang, A. Sha, Multifunctional application of nanoscratch technique to characterize cementitious materials, Cement Concr. Res. 140 (2021), 106318.
[11] J. Thomas, N.N. Thaickavil, P.M. Wilson, Strength and durability of concrete containing recycled concrete aggregates, J. Build. Eng. 19 (2018) 349–365.
[12] D. Pedro, J.d. Brito, L. Evangelista, Structural concrete with simultaneous incorporation of fine and coarse recycled concrete aggregates: mechanical, durability and long-term properties, Construct. Build. Mater. 154 (2017) 294–309.
[13] Z. Tang, Y. Hu, V.W.Y. Tam, W. Li, Uniaxial compressive behaviors of fly ash/slag-based geopolymeric concrete with recycled aggregates, Cem. Concr. Compos. 104 (2019), 103375.
[14] Y. Zaetang, V. Sata, A. Wongsa, P. Chindaprasirt, Properties of pervious concrete containing recycled concrete block aggregate and recycled concrete aggregate, Construct. Build. Mater. 111 (2016) 15–21.
[15] Z. Luo, W. Li, V.W.Y. Tam, J. Xiao, S.P. Shah, Current progress on nanotechnology application in recycled aggregate concrete, J. Sustain. Cem-Based Mater. 8 (2) (2019) 79–96.
[16] K. Wu, S. Luo, J. Zheng, J. Yan, J. Xiao, Influence of carbonation treatment on the properties of multiple interface transition zones and recycled aggregate concrete, Cem. Concr. Compos. 127 (2022), 104402.
[17] W. Li, J. Xiao, Z. Sun, S. Kawashima, S.P. Shah, Interfacial transition zones in recycled aggregate concrete with different mixing approaches, Construct. Build. Mater. 35 (2012) 1045–1055.
[18] J. Xiao, W. Li, Z. Sun, D.A. Lange, S.P. Shah, Properties of interfacial transition zones in recycled aggregate concrete tested by nanoindentation, Cem. Concr. Compos. 37 (2013) 276–292.
[19] B. Wang, L. Yan, Q. Fu, B. Kasal, A comprehensive review on recycled aggregate and recycled aggregate concrete, Resour. Conserv. Recycl. 171 (2021), 105565.
[20] S. Sunayana, S.V. Barai, Shear behavior of fly-ash-incorporated recycled aggregate concrete beams, ACI Mater. J. 117 (1) (2020) 289–303.
[21] Z. Tang, W. Li, V.W.Y. Tam, Z. Luo, Investigation on dynamic mechanical properties of fly ash/slag-based geopolymeric recycled aggregate concrete, Compos. B Eng. 185 (2020), 107776.
[22] L. Lin, J. Xu, J. Yuan, Y. Yu, Compressive strength and elastic modulus of RBAC: an analysis of existing data and an artificial intelligence based prediction, Case Stud. Constr. Mater. 18 (2023), e02184.
[23] Z. Tang, W. Li, V.W.Y. Tam, L. Yan, Mechanical performance of CFRP-confined sustainable geopolymeric recycled concrete under axial compression, Eng. Struct. 224 (2020), 111246.
[24] J. Jiang, P. Xiao, B. Li, True-triaxial compressive behaviour of concrete under passive confinement, Construct. Build. Mater. 156 (2017) 584–598.
[25] J. Xu, W. Chen, Y. Yu, J. Xu, X. Zhao, Data-driven analysis on compressive behavior of unconfined and confined recycled aggregate concretes, Construct. Build. Mater. 356 (2022), 129282.
[26] P. Folino, H. Xargay, Recycled aggregate concrete – mechanical behavior under uniaxial and triaxial compression, Construct. Build. Mater. 56 (2014) 21–31.
[27] Y. Chen, Z. Chen, J. Xu, E.M. Lui, B. Wu, Performance evaluation of recycled aggregate concrete under multiaxial compression, Construct. Build. Mater. 229 (2019), 116935.
[28] J. Xu, Y. Chen, T. Xie, X. Zhao, B. Xiong, Z. Chen, Prediction of triaxial behavior of recycled aggregate concrete using multivariable regression and artificial neural network techniques, Construct. Build. Mater. 226 (2019) 534–554.
[29] Y. Yang, C. Wu, Z. Liu, H. Zhang, 3D-printing ultra-high performance fiber-reinforced concrete under triaxial confining loads, Addit. Manuf. 50 (2022), 102568.
[30] Z. Deng, H. Huang, B. Ye, P. Xiang, C. Li, Mechanical performance of RAC under true-triaxial compression after high temperatures, J. Mater. Civ. Eng. 32 (8) (2020), 04020194.
[31] Y. Wu, C. Liu, G. Bai, H. Liu, Y. Meng, Z. Wang, 3D printed concrete with recycled sand: pore structures and triaxial compression properties, Cem. Concr. Compos. 139 (2023), 105048.
[32] W. Xue, X. Liu, W. Jing, Z. Yao, C. Gao, H. Li, Experimental study and mechanism analysis of permeability sensitivity of mechanically damaged concrete to confining pressure, Cement Concr. Res. 134 (2020), 106073.
[33] X.H. Vu, Y. Malecot, L. Daudeville, E. Buzaud, Experimental analysis of concrete behavior under high confinement: effect of the saturation ratio, Int. J. Solid Struct. 46 (2009) 1105–1120.
[34] Y. Malecot, L. Zingg, M. Briffaut, J. Baroth, Influence of free water on concrete triaxial behavior: the effect of porosity, Cement Concr. Res. 120 (2019) 207–216.
[35] T. He, T. Wang, D. Xie, J.J.K. Daemen, The mechanism of pores enhancing the deformation of completion cement under confining pressure, Cem. Concr. Compos. 125 (2022), 104322.
[36] J. Xiao, W. Li, D.J. Corr, S.P. Shah, Effects of interfacial transition zones on the stress–strain behavior of modeled recycled aggregate concrete, Cement Concr. Res. 52 (2013) 82–99.
[37] J.J. Xu, W.G. Chen, C. Demartino, T.Y. Xie, Y. Yu, C.F. Fang, M. Xu, A Bayesian model updating approach applied to mechanical properties of recycled aggregate concrete under uniaxial or triaxial compression, Construct. Build. Mater. 301 (2021), 124274.
[38] B. Lei, W. Yang, Y. Guo, X. Wang, Q. Xiong, K. Wang, W. Li, Interfacial adhesion between recycled aggregate and asphalt mastic filled with recycled concrete powder, Case Stud. Constr. Mater. 20 (2024), e02721.
[39] F. Qu, Y. Zhang, X. Zhu, W. Xu, C.S. Poon, W. Li, D.C.W. Tsang, Roles of wood waste biochar for chloride immobilization in GGBS-blended cement composites, Constr. Build. Mater. 411 (2024) 134389.
[40] B. Lei, L. Yu, Y. Guo, A.H. Mahmood, F. Qu, X. Wang, W. Li, Failure behaviour and damage evolution of multi-recycled aggregate concrete under triaxial compression, Eng. Fail. Anal. 153 (2023) 107572.
[41] Z. Luo, W. Li, K. Wang, A. Castel, S.P. Shah, Comparison on the properties of ITZs in fly ash-based geopolymer and Portland cement concretes with equivalent flowability, Cement Concr. Res. 143 (2021), 106392.
[42] Z. Luo, W. Li, K. Wang, S.P. Shah, D. Sheng, Nano/micromechanical characterisation and image analysis on the properties and heterogeneity of ITZs in geopolymer concrete, Cement Concr. Res. 152 (2022), 106677.
[43] H.S. Wong, M.K. Head, N.R. Buenfeld, Pore segmentation of cement-based materials from backscattered electron images, Cement Concr. Res. 36 (2006) 1083–1090.
[44] H.S. Wong, N.R. Buenfeld, Determining the water–cement ratio, cement content, water content and degree of hydration of hardened cement paste: method development and validation on paste samples, Cement Concr. Res. 39 (2009) 957–965.
[45] Z. Luo, W. Li, Y. Gan, X. He, A. Castel, D. Sheng, Nanoindentation on micromechanical properties and microstructure of geopolymer with nano-SiO2 and nano-TiO2, Cem. Concr. Compos. 117 (2021), 103883.
[46] Z. Luo, W. Li, Y. Gan, K. Mendu, S.P. Shah, Applying grid nanoindentation and maximum likelihood estimation for N-AS-H gel in geopolymer paste: investigation and discussion, Cement Concr. Res. 135 (2020), 106112.
[47] H.S. Wong, N.R. Buenfeld, Euclidean Distance Mapping for computing microstructural gradients at interfaces in composite materials, Cement Concr. Res. 36 (2006) 1091–1097.
[48] S. Diamond, J. Huang, The ITZ in concrete-a different view based on image analysis and SEM observations, Cem. Concr. Compos. 23 (2001) 179–188.
[49] K.L. Scrivener, A.K. Crumbie, P. Laugesen, The interfacial transition zone (ITZ) between cement paste and aggregate in concrete, Interface Sci. 12 (2004) 411–421.
[50] A.W. Pope, H.M. Jennings, The influence of mixing on the microstructure of the cement paste/aggregate interfacial zone and on the strength of mortar, J. Mater. Sci. 27 (1992) 6452–6462.
[51] Z. He, J. Zhang, Strength characteristics and failure criterion of plain recycled aggregate concrete under triaxial stress states, Construct. Build. Mater. 54 (2014) 354–362.
[52] Z. Xu, J. Li, P. Wu, C. Wu, Experimental investigation of triaxial strength of ultra-high performance concrete after exposure to elevated temperature, Construct. Build. Mater. 295 (2021), 123689.
[53] P. Vargas, O. Restrepo-Baena, J.I. Tobón, Microstructural analysis of interfacial transition zone (ITZ) and its impact on the compressive strength of lightweight concretes, Construct. Build. Mater. 137 (2017) 381–389.
[54] H. Zhang, X. Xu, W. Liu, B. Zhao, Q. Wang, Influence of the moisture states of aggregate recycled from waste concrete on the performance of the prepared recycled aggregate concrete (RAC) – a review, Construct. Build. Mater. 326 (2022), 126891.
[55] B. Li, S. Dai, Y. Zhan, J. Xu, X. Guo, Y. Yang, Y. Chen, Strength criterion of recycled aggregate concrete under triaxial Compression: model calibration, Construct. Build. Mater. 320 (2022), 126210.
[56] X. Jiang, Q. Li, X. Yin, S. Xu, Investigation on triaxial compressive mechanical properties of ultra high toughness cementitious composites with high strain capacity, Cement Concr. Res. 170 (2023), 107185.
[57] K.L. Scrivener, Backscattered electron imaging of cementitious microstructures: understanding and quantification, Cem. Concr. Compos. 26 (2004) 935–945.
[58] A. Jayasuriya, M.P. Adams, M.J. Bandelt, Understanding variability in recycled aggregate concrete mechanical properties through numerical simulation and statistical evaluation, Construct. Build. Mater. 178 (2018) 301–312.
[59] M.P. Collins, D. Mitchell, Prestressed Concrete Structures, Prentice Hall, Englewood Cliffs, NJ, 1991.
[60] Z. Guo, X. Zhang, D. Zhang, R. Wang, Experimental investigation of stress-strain curves for concrete, China, J. Build. Struct. 3 (1) (1982) 1–12.
[61] M. CE, Design of Concrete Structures, CEB-FIP Model Code, 1990.